Combustion and Flame 242 (2022) 112152

Contents lists available at ScienceDirect

Combustion and Flame

journal homepage: www.elsevier.com/locate/combustflame

Modelling of soot formation and aggregation in turbulent flows with the LES-PBE-PDF approach and a conservative sectional method

Binxuan Sun, Stelios Rigopoulos*

Department of Mechanical Engineering, Imperial College London, Exhibition Road, London SW7 2AZ, UK

ARTICLE INFO

Article history:
Received 31 March 2021
Revised 5 April 2022
Accepted 7 April 2022

Keywords:
Soot
Population balance
Sectional method
Turbulent flame
PDF method
Stochastic fields

ABSTRACT

The present paper presents a comprehensive approach for modelling soot formation in turbulent flows that incorporates a recently developed conservative finite volume sectional method for the solution of the population balance equation (PBE) into the Large Eddy Simulation - Probability Density Function (LES-PDF) framework for modelling turbulent reacting flows. The approach thus predicts the particle size distribution of soot and accounts for the complete set of aerosol dynamic processes (nucleation, surface growth, oxidation, condensation and aggregation) as well as for the interaction between turbulence, chemistry and soot. We employ a combination of gas-phase chemistry, soot kinetics and aerosol dynamics recently used by the authors in the context of a laminar co-flow diffusion flame and maintain the same kinetics without adjustments in order to focus on the modelling issues in turbulent sooting flame simulations. The results show that several features such as the location of the soot forming zones and the qualitative profiles of soot volume fraction and species concentrations can be predicted reasonably well, but there is a considerable underprediction in the magnitude of soot volume fraction. The possible reasons for this underprediction are discussed in the context of the aforementioned laminar flame simulation and the previous validation of the components of our methodology. The CPU time analysis shows that the solution of the PBE by the conservative sectional method and the associated transport of the discretised number densities account for less than 25% of the total CPU time, indicating that its incorporation in LES-PDF simulations of turbulent combustion is computationally feasible.

© 2022 The Author(s). Published by Elsevier Inc. on behalf of The Combustion Institute.
This is an open access article under the CC BY license (http://creativecommons.org/licenses/by/4.0/)

1. Introduction

Soot is polydisperse particulate matter formed during hydrocarbon combustion processes. It has severe consequences on human health [1], while it can also be desirable in certain cases such as furnace combustion, where it enhances heat transfer. In the past, it was mostly the total soot volume that was being controlled, while new regulations call for the control of the number of particles, especially for the smaller ones. Furthermore, nanoparticles such as carbon black used as advanced materials can be produced via flame synthesis [2] and control over the particle properties is essential for tailoring the product to specific applications. It is therefore becoming increasingly important to obtain accurate predictions of the soot particle size distribution in combustion processes.

The prediction of the particle size distribution is the objective of aerosol dynamics and requires the solution of the population balance equation (PBE), which is a methodology for modelling the evolution of distributed properties in systems undergoing kinetic processes such as nucleation, growth and aggregation, as well as transport processes. The simulation of sooting flames requires coupling of the PBE with the equations of fluid dynamics and scalar transport. While there are no fundamental impediments in carrying out this coupling in the context of laminar flows, turbulent flows bring new modelling challenges by introducing randomness into the distribution and unclosed terms into the PBE. Reviews of the issues related to the solution of the PBE and turbulence-soot interaction can be found in Refs. [3–5]. Recent advances have also shown that polycyclic aromatic hydrocarbons (PAHs) are of paramount importance in the process of soot formation [6], which means that detailed chemical mechanisms must be employed for their prediction. A comprehensive model of soot formation in turbulent flames must therefore include a number of components, namely accurate prediction of flow and turbulence, detailed gas-phase kinetics, aerosol dynamics models and an account for the interactions between all these elements.

Models for soot formation in non-premixed turbulent combustion include approaches based on Reynolds Averaged Navier Stokes

* Corresponding author.
E-mail address: s.rigopoulos@imperial.ac.uk (S. Rigopoulos).

https://doi.org/10.1016/j.combustflame.2022.112152
0010-2180/© 2022 The Author(s). Published by Elsevier Inc. on behalf of The Combustion Institute. This is an open access article under the CC BY license (http://creativecommons.org/licenses/by/4.0/)

(RANS), Large Eddy Simulation (LES) and Direct Numerical Simulation (DNS). RANS-based models have been the focus of sooting flame studies until the past decade, and a review of these works can be found in Ref. [5]. They have a low computational cost but rely heavily on modelling choices in order to account for the effect of turbulent fluctuations and for the interactions between turbulence, chemistry and soot, as the effects of fluctuations and nonlinear interactions at all scales must be accounted for by the models. DNS involves no modelling assumptions and provides detailed and complete datasets that are valuable for model development, but the high demands in CPU cost have limited its application to sooting flames to few studies dealing with simplified configurations and moderate Reynolds numbers [7–16]. In LES, the more energetic flow structures are resolved while modelling is used for the small scale processes. For this reason, LES is the most promising option for obtaining good predictions with affordable computational cost. LES-based studies of sooting flames and combustors have been appearing with increasing frequency, especially during the last decade (e.g. [9,10,17–34]). The applications of LES to reacting flows with soot differ in three main aspects, namely the modelling of turbulent-chemistry/soot formation interaction and subsequent closure strategy, the level of detail in soot kinetics and the formulation of aerosol dynamics.

With respect to aerosol dynamics, the PBE is a partial integro-differential equation and several methods have been developed for its solution including Monte Carlo, moment and discretisation (also called sectional) methods. Of these, mainly moment and, to a much smaller extent, sectional methods have been employed to simulations of turbulent sooting flames due to the need to keep the computational overhead at minimum. Moment methods are generally favoured because they involve the transport of just a few scalars (the moments of the distribution), although they require closure assumptions and do not predict the distribution directly. By contrast, sectional methods do not suffer from these limitations but are more computationally demanding. Still, some applications of them can be found in the context of RANS [35–41] and, lately, LES [27,28,34] simulations of turbulent sooting flows.

The first (to the authors' knowledge) LES of a turbulent non-premixed flame was conducted by El-Asrag and Menon [18], where a moment method for soot was included under the framework of the Linear Eddy Model (LEM) for the subfilter process. Later, Mueller and Pitsch [21] combined PAH inception kinetics and a moment-based soot model with an extended Flamelet/Progress Variable (FPV) model that accounts for radiative heat loss (RFPV) [42], and applied their approach to the Delft flame III [43]. The small-scale interaction between turbulence and soot was addressed by a presumed PDF method [19]. Specifically, the joint PDF was split into the PDF of the thermochemical variables and a conditional PDF of the soot scalars on the thermochemical variables, based on the assumption that the characteristic timescales related to soot precursors PAH and soot are much longer than that of the main heat-releasing thermochemical variables. Subsequently, the PDF of the thermochemical variables was modelled by a beta distribution for the mixture fraction and delta functions for variables related to progress variable and heat loss parameter, while a double delta function was used to model the soot-related PDF. To accommodate the slow chemistry of PAH, the authors added a separate transport equation for a lumped PAH mass fraction. In a subsequent study, Xuan and Blanquart [10] solved the filtered transport equations for benzene (C_6H_6) and naphthalene ($C_{10}H_8$) as an alternative approach to the lumped PAH evolution equation in [21]. The associated closure for the filtered source terms was achieved by a PAH relaxation model. As the soot evolution in these studies was described by moment-based method, no information on the soot distribution was predicted. A recent study by Rodrigues et al. [28] applied a soot sectional method within the scope of LES-presumed PDF model of Mueller and Pitsch [21], in which some qualitative trends in soot measurements were reproduced.

Another mixture fraction-based method that has been employed in soot modelling is the LES-Conditional Moment Closure approach. In an early study, Navarro-Martinez and Rigopoulos [20] incorporated a two-equation semi-empirical soot model of Leung et al. [44] into an LES-CMC framework to model a turbulent non-premixed flame. Recently, the LES-CMC approach and the two-equation soot model were employed to study soot formation in a single sector model combustor by Giusti et al. [29]. Both studies assumed a presumed β-function to compute unconditional filtered values. A more recent work by Grader et al. [34] employed a presumed-PDF method with LES and a sectional method for the simulation of a lifted non-premixed turbulent flame. Measurements of sooting flames often do not provide joint data, which is a significant challenge for model validation [9]. In turbulent flow, PAH species related to soot precursors are highly sensitive to turbulent mixing and scalar dissipation rate [7,8], while their chemical reaction rates are relatively slow and do not respond promptly to the mixing phenomena [12]. In a recent work by Wick et al. [15], errors in soot predictions associated with flamelet-based combustion models were analysed comprehensively with the help of DNS, and the largest uncertainties were attributed to the PAH chemical mechanism and the modelling of PAH source term.

The studies mentioned above are based on various forms of presumed PDF methods or CMC, in which a small number of variables such as mixture fraction and progress variable are being transported while models are employed for the unclosed terms associated with the turbulence-chemistry and turbulence-soot interaction. By contrast, transported PDF methods [45–48] were developed with the aim to bring the unclosed terms relating to turbulence-chemistry interaction to a closed form. This is attained by solving an equation for the joint PDF of the reacting scalars. The resulting equation still contains two unclosed terms due to turbulent transport and micromixing. The first of these may be addressed by a joint velocity-scalar PDF method [46] or modelled via a gradient transport model. The second one represents the main closure challenge in PDF methods, and a number of models have been developed for that purpose [46–48]. Another issue with transported PDF methods is the increase in the number of independent variables, which now includes the variables whose joint PDF is considered. For this reason, conventional discretisation methods cannot be employed and some form of Monte Carlo method must be employed. RANS-PDF simulations were based mostly on the method of Lagrangian stochastic particles [46], where a number of virtual particles with different compositions are transported and the distribution of composition among the particles at each location is used to represent the PDF. In LES, an alternative method that is being increasingly employed is the stochastic field method [49–51], where the PDF is represented by an ensemble of continuous fields. In the context of LES and stochastic fields, the Interaction with the Mean (IEM) [52,53] is the main micromixing model that has been employed. Unlike models based on jump processes such as Curl's model and variants thereof, the IEM model provides continuous and differentiable solutions.

The concept of transported PDF methods was extended to reacting flows with particles via the PBE-PDF approach [54], where an evolution equation for the one-point, one-time joint probability density function associated with reactive scalars and the particle number density is introduced. The PBE-PDF equation accounts for the unclosed terms resulting from turbulence-chemistry-soot interaction that can be divided into three types: functions of reactive scalars, such as nucleation, terms involving correlations of scalars and number density, such as surface growth, and terms involving products of number densities, such as aggregation and condensation. Furthermore, the method is inherently coupled

with a sectional approach because the PBE is first discretised and the sectional number densities function as the variables for the PDF. Initially, the approach was developed in the context of RANS and coupled with the stochastic particle method [55,56]. The PBE-PDF approach was later extended to LES and combined with the stochastic field method [57]. The LES-PBE-PDF approach was first applied to a sooting flame in combination with a simplified soot model [27]. The transported PDF approach has also been employed in two-dimensional parabolic RANS computations together with a sectional method for modelling turbulent sooting flames [39–41]. Finally, transported PDF frameworks have also been combined with simplified soot models [58–61] and moment methods [60,62] in RANS and also with moment methods in an LES simulation with the RFPV flamelet-based model [22].

The present paper has two main objectives. First, we introduce a complete physicochemical model of soot formation including comprehensive gas-phase kinetics including PAH formation [63], a detailed PAH-based soot kinetic model [64] and particle aggregation into the LES-PBE-PDF modelling framework. The sectional method employed is a recently proposed conservative finite volume method that emphasises accuracy and conservation of moments in the discretisation of aggregation [65]. Second, we perform the simulation of a turbulent non-premixed sooting flame, the Sandia ethylene flame [66], by employing the same set of models for gas-phase chemistry, soot kinetics and aerosol dynamics that was recently employed by the authors in the context of a laminar co-flow diffusion flame [67] without any adjustments in parameters. Among laminar flame configurations, the co-flow diffusion flame requires the full coupling of PBE with an unsteady CFD code and thus its simulation bears the closest resemblance to the turbulent flame simulation performed here. By maintaining the same description of kinetics and aerosol dynamics for both the laminar and the turbulent flame, we aim to shed light to the nature of discrepancies that arise in the simulation of turbulent sooting flames. The paper is organized as follows. First, the LES-PBE-PDF formalism is summarised, followed by a summary of the models employed for kinetics and aerosol dynamics. Subsequently, the turbulent flame configuration and numerical setup are presented, and model predictions are compared with experimental measurements. This is followed by a discussion of results and an investigation of the underlying mechanisms, before summarising the conclusions drawn in this work.

2. The LES-PBE-PDF model formulation for turbulent reacting flows with particle formation

2.1. Equations of reacting flows with particle formation

The PBE describes the evolution of the soot particle size distribution as a result of transport and aerosol processes. In a perfectly stirred reactor, the PBE can be written as follows:

$$\begin{aligned}\frac{dN'(v,t)}{dt} = &-\frac{\partial(G(\mathbf{Y},v)N'(v,t))}{\partial v} \\ &+ B(\mathbf{Y})\delta(v-v_0) + C(\mathbf{Y},N'(v,t)) \\ &+ \frac{1}{2}\int_0^v \beta(w,v-w)N'(w,t)N'(v-w,t)dw \\ &- \int_0^\infty \beta(v,w)N'(v,t)N'(w,t)dw \end{aligned} \tag{1}$$

where a volume-based distribution is employed, such that $N'(v,t)$ is the particle number density per unit volume of mixture as a function of particle volume and time. The functions G, B and C yield the rates of particle growth/oxidation, nucleation and condensation respectively, and involve the concentrations of reactive species, Y_k, while the function β is the aggregation kernel. The detailed forms of these terms depend on the kinetic models employed, which will be discussed in Section 3.

In order to couple the PBE with fluid dynamics, we introduce a space-dependent distribution, $N(v,\mathbf{x},t)$. Furthermore, anticipating the application of the PBE to variable density flows, we consider the number density of particles per unit of mixture mass, such that $N = N'/\rho$. The spatially dependent PBE can be written in Cartesian coordinates as follows (for brevity, the dependent variables will be omitted in the following wherever possible):

$$\frac{\partial \rho N}{\partial t} + \frac{\partial(\rho u_j N)}{\partial x_j} = -\frac{\partial K_j}{\partial x_j} + \dot{s}(v,\mathbf{Y},N) \tag{2}$$

where the source term, $\dot{s}(v,\mathbf{Y},N)$, accounts for the chemical and aerosol processes that appear in Eq. (1). The soot particles are being transported via convection by the gas and diffusion, while thermophoresis can be neglected for turbulent flows. Diffusion is described by the diffusive flux, K_j, as follows:

$$\begin{aligned}K_j(v,\mathbf{x},t) &= -D_p(v,\mathbf{x},t)\frac{\partial(N'(v,\mathbf{x},t))}{\partial x_j} \\ &= -D_p(v,\mathbf{x},t)\frac{\partial(\rho N(v,\mathbf{x},t))}{\partial x_j}\end{aligned} \tag{3}$$

where $D_p(v,\mathbf{x},t)$ denotes the particle diffusivity and is a function of particle size, according to the Stokes-Einstein equation [68].

The PBE must be coupled with the conservation equations for mass, momentum, species and enthalpy transport. For low Mach number flows, these can be written as follows:

$$\frac{\partial \rho}{\partial t} + \frac{\partial(\rho u_j)}{\partial x_j} = 0 \tag{4}$$

$$\frac{\partial \rho u_i}{\partial t} + \frac{\partial(\rho u_i u_j)}{\partial x_j} = -\frac{\partial p}{\partial x_i} + \frac{\partial \tau_{ij}}{\partial x_j} + \rho g_i \tag{5}$$

$$\frac{\partial \rho Y_k}{\partial t} + \frac{\partial(\rho u_j Y_k)}{\partial x_j} = -\frac{\partial J_{kj}}{\partial x_j} + \rho\dot{\omega}_k(\mathbf{Y},N) \tag{6}$$

where τ_{ij}, g_i and $\dot{\omega}_k(\mathbf{Y},N)$ represent the viscous stress tensor, the gravitational acceleration and the chemical reaction source term (which depends on the species mass fractions and the number density, as the consumption of reacting species depends on the particle surface area), respectively, while J_{kj} denotes the diffusive flux of a reactive scalar, Y_k:

$$J_{kj}(\mathbf{x},t) = -\rho D_m(\mathbf{Y}(\mathbf{x},t))\frac{\partial Y_k(\mathbf{x},t)}{\partial x_j} \tag{7}$$

where $D_m(\mathbf{Y}(\mathbf{x},t))$ denotes the kinematic diffusivity of any scalar into the mixture and can be related to the mixture kinematic viscosity, μ, via the Schmidt number such that $\rho D_m = \mu/Sc$ [69]. The enthalpy transport equation is written in terms of the total enthalpy, which includes the enthalpies of formation, and therefore the corresponding transport equation assumes the same form as Eq. (6) with a source term accounting for radiative heat transfer and a diffusion term involving the Prandtl number. In our study, the carrier fluid is treated as a multicomponent ideal gas, and its mixture density, $\rho(\mathbf{Y})$, is a function of the local values of the reactive scalars.

2.2. Filtered Navier-Stokes equations

Using conventional filtering operations for low-Mach number variable density flows, the LES-filtered conservation equations for mass and momentum are written as [69]:

$$\frac{\partial \overline{\rho}}{\partial t} + \frac{\overline{\rho}\widetilde{u}_j}{\partial x_j} = 0 \tag{8}$$

$$\frac{\partial \overline{\rho}\widetilde{u}_i}{\partial t} + \frac{\partial \overline{\rho}\widetilde{u}_i\widetilde{u}_j}{\partial x_j} = -\frac{\partial \overline{p}}{\partial x_i} + \frac{\partial (\widetilde{\tau}_{ij} - \tau^*_{ij})}{\partial x_j} + \overline{\rho} g_i \tag{9}$$

where the operator $\overline{\cdot}$ indicates filtering and the operator $\widetilde{\cdot}$ indicates the density weighted (Favre) filtering. Moreover, $\widetilde{\tau}_{ij}$ denotes the resolved viscous stress tensor associated with the Favre-filtered velocity field $\widetilde{\mathbf{u}}(\mathbf{x}, t)$ [69] and $\tau^*_{ij} = \overline{\rho}(\widetilde{u_i u_j} - \widetilde{u}_i\widetilde{u}_j)$ represents the sub-grid scale (SGS) stress tensor, which involves the unresolved SGS term and thus requires modelling. In the present study, we adopt the standard Smagorinsky model [70] for the deviatoric part of the SGS stress tensor:

$$\tau^*_{ij} - \frac{\delta_{ij}}{3}\tau^*_{kk} = -2\mu_{sgs}\widetilde{e}_{ij} \tag{10}$$

with the SGS turbulent viscosity μ_{sgs}:

$$\mu_{sgs} = \overline{\rho}(C_S\Delta)^2\left|\left|\widetilde{e}_{ij}\right|\right| \tag{11}$$

where $||\widetilde{e}_{ij}|| = \sqrt{2\widetilde{e}_{ij}\widetilde{e}_{ij}}$ is the Frobenius norm of the resolved rate of strain tensor, $\widetilde{e}_{ij} = 0.5(\frac{\partial \widetilde{u}_i}{\partial x_j} + \frac{\partial \widetilde{u}_j}{\partial x_i})$, and the Smagorinsky constant is $C_S = 0.1$. For both the resolved and SGS stresses, the isotropic part is absorbed into the pressure [69]. While the experimental dataset to be simulated in the present study does not offer velocity predictions, the LES model and parameter choices are the same as in the work of Sewerin and Rigopoulos [27], which used the same code for a sooting jet flame and where the flow field predictions agreed well with the experimental data.

2.3. Joint scalar-number density PDF

Applying the filtering operation to the transport equations of the reactive scalars (Eq. (6)) and number densities (Eq. (2)) would result in the unclosed source terms $\overline{\dot{\omega}(\mathbf{Y}, N)}$ and $\overline{\dot{s}(\nu, \mathbf{Y}, N)}$, as $\overline{\dot{\omega}(\mathbf{Y}, N)} \neq \dot{\omega}(\overline{\mathbf{Y}}, \overline{N})$ and $\overline{\dot{s}(\mathbf{Y}, N)} \neq \dot{s}(\nu, \overline{\mathbf{Y}}, \overline{N})$. The first of these terms is related to turbulence-chemistry interaction. The second one denotes turbulence-chemistry-soot interaction, and the correlations associated with it result from non-linear functions of species concentrations and number density. These terms have been discussed in Ref. [54], where the PBE-PDF method was proposed to bring closure to them, initially in the context of RANS. The derivation of the LES-PBE-PDF method was first shown in Ref. [57] in the context of constant density flows and subsequently in Ref. [27] for variable density flows, based on the concepts of LES-PDF methods for reacting flows pioneered by Gao and O'Brien [71], hence only the main points will be shown here.

Before defining the joint scalar-number density PDF, we first introduce a discretised form of the number density by applying a sectional method. The choice of method is irrelevant here, and what matters is the fact that the number density function, which is a continuous function of particle volume, can be represented by an array of m scalars, $N_i(\mathbf{x}, t)$, each of them denoting the number density of particles within a section i with volume in the range (v_{i-1}, v_i). As a start, we follow the standard practice of first introducing the concept of one-point, one-time, Eulerian fine-grained PDF $g(\mathbf{y}, \mathbf{n}; \mathbf{x}, t)$ for the joint reactive scalars and particle number densities, where y_k and n_i denote the domain of definition of Y_k and N_i respectively. This function is defined such that $g(\mathbf{y}, \mathbf{n})d\mathbf{y}d\mathbf{n}$ is the joint probability that at position $\mathbf{x}$ and time t, $y_k \leq Y_k(\mathbf{x}, t) \leq y_k + dy_k$ for all $k = 1, \ldots, n_s$, and $n_i \leq N_i(\mathbf{x}, t) \leq n_i + dn_i$ for all $i = 1, \ldots, m$, formulated as:

$$\begin{aligned} g(\mathbf{y}, \mathbf{n}; \mathbf{x}, t) &= \prod_{k=1}^{n_s}\prod_{i=1}^{m}\delta(y_k - Y_k(\mathbf{x}, t))\delta(n_i - N_i(\mathbf{x}, t)) \\ &= \delta(\mathbf{y} - \mathbf{Y}(\mathbf{x}, t))\delta(\mathbf{n} - \mathbf{N}(\mathbf{x}, t)) \end{aligned} \tag{12}$$

where y_k and n_i denote independent variables and represent the sample space of the dependent random variables Y_k and N_i, respectively; $\mathbf{Y}$ and $\mathbf{N}$ denote the set of Y_k for all $k = 1, \ldots, n_s$ and N_i for all $i = 1, \ldots, m$, respectively. Following Ref. [27], the joint scalar-number density PDF can be formulated under the framework of LES as follows:

$$\begin{aligned} f_{\mathbf{Y},\mathbf{N}}(\mathbf{y}, \mathbf{n}; \mathbf{x}, t) &= \overline{g(\mathbf{y}, \mathbf{n}; \mathbf{x}, t)} \\ &= \overline{\delta(\mathbf{y} - \mathbf{Y}(\mathbf{x}, t))\delta(\mathbf{n} - \mathbf{N}(\mathbf{x}, t))} \\ &= \int_\Omega G(\mathbf{x} - \mathbf{x}')\delta(\mathbf{y} - \mathbf{Y}(\mathbf{x}', t))\delta(\mathbf{n} - \mathbf{N}(\mathbf{x}', t))d\mathbf{x}' \end{aligned} \tag{13}$$

The joint scalar-number density PDF in the context of LES can be seen as a cell-averaged representation of a single realisation, such that its integral over a finite region of its sample space represents the likelihood of occurrence of a certain set of concentrations and particle size distribution within a cell. In particular, $f_{\mathbf{Y},\mathbf{N}}$ represents the joint probability of $\mathbf{Y} = \mathbf{y}$ and $\mathbf{N} = \mathbf{n}$ arising within the filter volume. For a positive definite filter, it can be shown that the $f_{\mathbf{Y},\mathbf{N}}$ has the properties of a PDF. The LES-filtering of the non-linear source terms $\dot{\omega}(\mathbf{Y}, \mathbf{N})$ and $\dot{s}(\mathbf{Y}, \mathbf{N})$ can therefore be performed as follows:

$$\begin{aligned} \overline{\dot{\omega}}(\mathbf{Y}, \mathbf{N}; \mathbf{x}, t) &= \int_\Omega G(\mathbf{x} - \mathbf{x}')\dot{\omega}(\mathbf{Y}(\mathbf{x}', t), \mathbf{N}(\mathbf{x}', t))d\mathbf{x}' \\ &= \int_\Omega G(\mathbf{x} - \mathbf{x}')\left(\int_{-\infty}^{\infty}\dot{\omega}(\mathbf{y}, \mathbf{n})g(\mathbf{y}, \mathbf{n}; \mathbf{x}', t)d\mathbf{y}d\mathbf{n}\right)d\mathbf{x}' \\ &= \int_{-\infty}^{\infty}\dot{\omega}(\mathbf{y}, \mathbf{n})\left(\int_\Omega G(\mathbf{x} - \mathbf{x}')g(\mathbf{y}, \mathbf{n}; \mathbf{x}', t)d\mathbf{x}'\right)d\mathbf{y}d\mathbf{n} \\ &= \int_{-\infty}^{\infty}\dot{\omega}(\mathbf{y}, \mathbf{n})f_{\mathbf{Y},\mathbf{N}}(\mathbf{y}, \mathbf{n}; \mathbf{x}, t)d\mathbf{y}d\mathbf{n} \end{aligned} \tag{14}$$

and likewise for $\dot{s}(\mathbf{Y}, \mathbf{N})$. In the above, we have used the sifting property of the delta function and subsequently interchanged the order of integration. Therefore, once the joint scalar-number density PDF is known, the filtered source terms appear in closed form, in spite of their non-linear dependence on the scalar fields $\mathbf{Y}$ and $\mathbf{N}$. This includes the integral terms in the PBE, where the source of the closure issue lies in the non-linearity of the products of number densities. The reader may consult Ref. [57] for more details.

Following the derivation in Ref. [27], the transport equation for the density-weighted joint scalar-number density PDF, $\widetilde{f}_{\mathbf{Y},\mathbf{N}}(\mathbf{y}, \mathbf{n}; \mathbf{x}, t)$ can be written as:

$$\begin{aligned} \overline{\rho}\frac{\partial \widetilde{f}}{\partial t} + \overline{\rho}\widetilde{u}_j\frac{\partial \widetilde{f}}{\partial x_j} &= \frac{\partial}{\partial x_j}\left(\overline{\rho}\Gamma\frac{\partial \widetilde{f}}{\partial x_j}\right) \\ &\quad - \sum_{k=1}^{n_s}\frac{\partial}{\partial y_k}\left(\overline{\rho}\dot{\omega}_k(\mathbf{y}, \mathbf{n})\widetilde{f} - \frac{\overline{\rho}\widetilde{f}}{\rho}\overline{\left(\frac{\partial J_{kj}}{\partial x_j}\middle|\mathbf{y}, \mathbf{n}\right)}\right) \\ &\quad - \sum_{i=1}^{m}\frac{\partial}{\partial n_i}\left(\frac{\overline{\rho}\widetilde{f}}{\rho}\dot{s}_i(\mathbf{y}, \mathbf{n}) - \frac{\overline{\rho}\widetilde{f}}{\rho}\overline{\left(\frac{\partial K_{ij}}{\partial x_j}\middle|\mathbf{y}, \mathbf{n}\right)}\right) \end{aligned} \tag{15}$$

where K_{ij} denotes the diffusive flux associated with number density N_i, and we omit the subscript symbols in the PDF $\widetilde{f}$ for brevity. The scaled turbulent kinematic viscosity, $\Gamma = \mu_{sgs}/(\overline{\rho}Sc)$, is modelled via the SGS turbulent viscosity computed by Eq. (11). The turbulent transport is modelled via a gradient diffusion hypothesis [27]. We employ a constant turbulent Schmidt/Prandtl number $Sc = 0.7$; as with the other modelling and parameter choices, this is guided by previous studies of turbulent jet flames with LES-PDF methods and the same code [69]. The molecular diffusivity contribution is addressed in Section 2.4.

In Eq. (15), the non-linear source terms $\dot{\omega}_k$ and $\dot{s}_i$, which represent the discretised form of the right-hand side of Eq. (1), are in closed form, thus accounting for the interaction between turbulence, chemistry and soot without the need for further closure assumptions. The only further closure required is for the micromixing terms for the reactive scalars and the number densities, i.e. $\overline{(\frac{\partial J_{kj}}{\partial x_j}|\mathbf{y},\mathbf{n})}$ and $\overline{(\frac{\partial K_{ij}}{\partial x_j}|\mathbf{y},\mathbf{n})}$. These unclosed terms represent the molecular diffusion of the PDF in the sample space. The model for their closure is presented in the next section.

2.4. Micromixing model

There are two aspects of molecular diffusion to be considered: one is the process of mixing, which appears as transport in reactive scalar and number density space in the PDF, and the other one is spatial transport, which appears as gradient diffusion of the PDF in physical space. A number of proposals have been made for closing the micromixing terms [72,73]. In our work, the associated closure is achieved by an augmented IEM micromixing model proposed initially by McDermott and Pope [74] and employed into the LES-PBE-PDF approach by Sewerin and Rigopoulos [27,57]:

$$-\frac{1}{\rho}\overline{\left(\frac{\partial J_{kj}}{\partial x_j}\middle|\mathbf{y},\mathbf{n}\right)} = \kappa(\mathbf{x},t)(\tilde{Y}_k - y_k) + \frac{1}{\overline{\rho}}\frac{\partial}{\partial x_j}\left(\overline{\rho}\tilde{D}_m\frac{\partial \tilde{Y}_k}{\partial x_j}\right) \tag{16}$$

$$-\frac{1}{\rho}\overline{\left(\frac{\partial K_{ij}}{\partial x_j}\middle|\mathbf{y},\mathbf{n}\right)} = \kappa(\mathbf{x},t)(\tilde{N}_i - n_i) + \frac{1}{\overline{\rho}}\frac{\partial}{\partial x_j}\left(\tilde{D}_{p,i}\frac{\partial \overline{\rho}\tilde{N}_i}{\partial x_j}\right) \tag{17}$$

where $\kappa(\mathbf{x},t)$ denotes a micromixing frequency common to all scalars:

$$\kappa(\mathbf{x},t) = \frac{C_\kappa}{2}\frac{\Gamma(\mathbf{x},t)}{\Delta^2} \tag{18}$$

where the SGS mixing constant $C_\kappa = 2$, and Δ is the characteristic width defined in the context of LES. Formally, Eq. (17) provides the closure of the transport equation of the joint scalar-number density PDF (Eq. (15)). This model accounts for the spatial transport of the PDF and consequently accounts for the spatial transport of all moments of the PDF. The decay of the SGS covariance can also be captured, as indicated in [74]. In order to guarantee that the SGS covariance vanishes in the DNS limit, i.e. that the micromixing frequency $\kappa(\mathbf{x},t) \to \infty$ as the grid resolution approaches the Kolmogorov scale, we introduce a scaling, which relates the turbulent viscosity to the molecular viscosity [75]:

$$\kappa^*(\mathbf{x},t) = \kappa(\mathbf{x},t)\frac{1+\frac{\mu_{sgs}}{\mu}}{\frac{\mu_{sgs}}{\mu}} \tag{19}$$

This scaling ensures an increased micromixing frequency in regions where the flame is well resolved. It only becomes effective if the turbulent viscosity is small compared to the molecular viscosity. In high Reynolds number flows, where the flame is typically located in an unresolved region, the turbulent viscosity is large compared to the molecular viscosity and the scaling has no significant effect.

The modelling of micromixing is the most important assumption in transported PDF methods. In RANS-PDF methods, the model and the corresponding constant determine the decay rate of, for example, mixture fraction variance and this can have a profound effect in RANS combustion modelling. In LES, the variance of scalar quantities is resolved and the mixing model determines the subgrid-scale scalar variance. As the energetic motions are resolved in LES, the representation of micromixing at the subgrid scale provided by the IEM model may be adequate in many practical situations [76], and this model has been extensively used in studies of turbulent flames with the LES-PDF approach (see, for example, Jones and Prasad [69]). It must be noted, however, that the diffusivity of soot is much smaller than that of gas-phase species. At the grid level, differential diffusion of both species and soot is considered (the diffusivity of the latter is calculated with the Stokes-Einstein equation), but this effect cannot be accounted for at the subgrid scale via the standard IEM model. In the present study, in accordance with the premise of employing the models without adjustments, we employ the IEM model with the same form and micromixing frequency as used in the majority of turbulent flame simulations. It must be acknowledged, however, that the modelling of micromixing for soot is an open problem for the time being and should be addressed in future work, ideally via the development of an improved micromixing model.

2.5. Method of stochastic fields

Due to the high dimensionality of Eq. (15), obtaining its solution via standard finite-difference or finite-volume solution methods is computationally intractable. Therefore, we adopt the Monte Carlo method for the solution of the joint scalar-number density PDF. Our primary goal is to estimate the average values of scalars and number densities, rather than to accurately compute the joint species-number density PDF. Several stochastic solution methods have been developed for dealing with PDF methods, such as the Eulerian stochastic particle method [77], the Lagrangian stochastic particle method [46] and the method of stochastic fields [49–51] (which is Eulerian). Sewerin and Rigopoulos [27,57] adapted the stochastic fields method to the LES-PBE-PDF approach, and this formulation will be employed in the present work.

The main concept underlying the Eulerian stochastic fields method is the construction of a system of stochastic differential equations (SDEs), statistically equivalent to the closed form of the transport equation of the joint PDF. The final system of SDEs is derived using Itô calculus [78] and is shown below, while the detailed derivation can be found in Refs. [27,57]:

$$\begin{aligned}\overline{\rho}d\theta_\alpha^l = &-\overline{\rho}\widetilde{u}_j\frac{\partial\theta_\alpha^l}{\partial x_j}dt + \frac{\partial}{\partial x_j}\left(\overline{\rho}\Gamma\frac{\partial\theta_\alpha^n}{\partial x_j}\right)dt \\ &- \overline{\rho}\sqrt{2\Gamma}\frac{\partial\theta_\alpha^l}{\partial x_j}dW_j^n(t) + \overline{\rho}\left(\dot{\omega}_\alpha^l(\boldsymbol{\theta},\mathbf{x}) + m_\alpha^l(\boldsymbol{\theta},\mathbf{x})\right)dt\end{aligned} \tag{20}$$

where θ_α^l is the value of a scalar α, which can be either a species mass fraction or discretised number density (hence $\alpha = 1, n_s + m$), associated with field l (where $l = 1, n_f$). Furthermore, $\dot{\omega}_\alpha^l$ is the reactive source term and m_α^l is the micromixing term, both associated with scalar α and field l, while $\dot{W}_j^l(t)$ is the increment of three-dimensional Wiener process in the jth direction for field l. By construction, the filtered values of any scalar, $\tilde{Z}_k$, can then be computed via an average over the field values.

$$\widetilde{Z}_k = \frac{1}{n_f}\sum_{l=1}^{n_f}\theta_\alpha^l \tag{21}$$

3. Models for chemical kinetics and aerosol dynamics

3.1. Gas-phase chemistry and radiation

The objective of this study is to simulate a turbulent flame with the same set of kinetics employed in Ref. [67] for the simulation of the Santoro laminar co-flow diffusion flame. These include a mechanism for gas phase chemistry due to Blanquart et al. [63]. The mechanism was developed with focus on the important species for soot formation (e.g., acetylene, the C_3H_4 isomers, propene and butadiene) and contains 149 species and 1651 reactions, accounting for the formation of larger PAH species up to $C_{18}H_{10}$. The complete

mechanism has been validated for a large set of fuels in laminar premixed and counterflow diffusion flames. An optically thin radiation model is employed, further information on which can be found in e.g. Modest [79], and the implementation is the same as in Refs. [27,67].

3.2. Soot kinetics and aerosol dynamics

The soot kinetics employed are also the same as in Ref. [67], which employed the model due to Blanquart and Pitsch [64]. The nucleation and condensation models involve the formation of intermediate dimers. Eight PAHs are considered to be responsible for the formation of dimers, and the collision between dimers results in the formation of soot nuclei. Furthermore, condensation is considered to result from collisions between soot particles and dimers. Since dimers are assumed to be in a quasi-steady state, the dimer production rate due to PAH dimerisation equals the dimer consumption rate due to soot nucleation and condensation and a quadratic equation can be solved to determine the concentration of dimers [64]. The soot surface growth and oxidation are modelled via the H-abstraction/C_2H_2 addition (HACA) mechanism, pioneered by Frenklach and Wang [80]. The implementation details are the same as in Ref. [67].

For the modelling of soot aggregation, the free molecule, transition and continuum regimes and transition regimes are all accounted for. The focus of Ref. [67] was on soot aggregation, where a more advanced method was developed based on a two-population balance model and the conservative finite volume method (CFV-2PBE). The aim of that method was to improve on the approach of modelling soot aggregates with a single PBE (CFV-1PBE), which is based on the assumption of a cut-off size between primary particles and aggregates. It was shown that the CFV-2PBE method improved on CFV-1PBE mainly on the prediction of variables associated with soot aggregate structure, but not so much on the prediction of soot volume fraction and temperature. In the present study, we choose to employ the CFV-1PBE method for several reasons: a) the experimental dataset that we will compare with contains no other information on soot than volume fraction, b) the CFV-1PBE method involves fewer PBE scalars and is thus less expensive, and c) the experimental information on the fusing of soot primary particles is still at a primitive stage to allow for the full potential of the two-PBE approach to be realised [67].

In the CFV-1PBE model, particles smaller than the cut-off size are assumed to be spherical, while particles larger than that are assumed to have fractal shapes with equally sized primary particles whose diameter, d_p, is equal to the cut-off size. Subsequently, the collision diameter $d_g(v)$ used in the calculation of aggregation kernel β can be related to the particle volume as follows:

$$\frac{v}{v_p} = k_f \left(\frac{d_g(v)}{d_p} \right)^{D_f} \tag{22}$$

where v_p is the volume of the primary particles, k_f is the fractal prefactor taken to be equal to 1.94 [81] and D_f is the fractal dimension for which a value of 1.8 is used [82,83]. These values, as well as all other model parameters in the present study, are the same as those used in our simulation of the laminar Santoro flame [67]. In particular, the cut-off point is 30.8 nm and the surface reactivity, α, is computed according to $\alpha = 0.0037 e^{9000/T}$.

4. Numerical methods

The LES-PBE-PDF method with soot formation for simulating turbulent reacting flow was implemented in our in-house CFD code LES-BOFFIN [84], which is based on a variable-density low Mach number formulation of the three-dimensional Navier-Stokes equations. For the coupled LES-filtered mass and momentum equations (Eqs. (8) and (9)), we adopt a second-order accurate finite volume scheme on a staggered grid. For the reactive scalars, the transport equations for the stochastic fields (Eq. (20)) are solved with a fractional step method. Similarly, the stochastic field equation for the population balance involves a convection/diffusion, micromixing and PBE fractional step. A schematic illustration of the overall LES-PBE-PDF code implementation is shown in Fig. 1.

The aerosol dynamics solver is the conservative finite volume sectional method developed by Liu and Rigopoulos [65]. An important feature of this method is that it conserves the first moment (which is proportional to the soot mass and thus important for the mass balance) during the aggregation processes, while placing no restriction on the structure of the non-uniform grid employed in the particle volume domain. The method has been shown to provide accurate solutions for the particle size distribution with reasonable CPU requirements when incorporated within a CFD code [65]. In order to maintain the same implementation as in Ref. [67], 60 sections are used to cover a particle size range from 0.72 nm to 1.24 μm.

In the convection/diffusion fractional step, the convective terms are discretised via a TVD scheme based on van Leer's limiter; the spatial diffusion terms combine the diffusion due to turbulent transport and the diffusion due to micromixing and are discretised by the central difference scheme. A second-order accurate Crank-Nicolson method is applied for the temporal integration of the deterministic terms, while an Euler-Maruyama scheme [78] is adopted for the stochastic terms. For the chemical reaction fractional step, a first-order accurate implicit Euler method is used. The temporal integration of the PBE fractional step is achieved via an explicit Euler method as the PBE step is not stiff. The reaction mechanism is hard-coded in order to accelerate the solution process. Finally, a recently developed dynamic load balancing scheme [85] is applied to the reaction fractional step for better efficiency when running the code in massively parallel computing systems. Cumulatively, all these techniques achieve a reduction in the runtime of the reaction fractional step by approximately one order of magnitude.

5. Flame configuration and numerical setup

The flame to be simulated is the Sandia ethylene flame, and the design of this rig was first described by Zhang et al. [66]. The flame has a central fuel jet surrounded by two concentric tubes of pilot flame and air. The fuel jet has an inner diameter (ID) of 3.2 mm and an outer diameter (OD) of 4.6 mm, and it is encircled by the pilot of ID 15.2 mm and OD 19.1 mm. Ethylene at room temperature 295 K is injected with bulk velocity $V_{fuel} = 54.7$ m/s in the central nozzle, resulting in a Reynolds number of 20,000. The pilot consists of premixed ethylene and air at an equivalence ratio of 0.9 and the flow rate of the pilot mixture is adjusted such that the heat release corresponds to 2% of that of the fuel jet. An adiabatic flame temperature is imposed for the corresponding equivalence ratio. The pilot is surrounded by a co-flow of air at 295 K and a uniform velocity $V_{air} = 0.6$ m/s. The experiment was conducted under an atmospheric pressure.

The computational domain is a rectangular parallelepiped, spanning 900 mm in the axial x-direction and 300 mm in the y and z directions with 240, 80 and 80 cells respectively. The grid is stretched by a factor of 1.013 axially, resulting in higher resolution near the burner. Radially, ten cells are allocated in the central region to resolve the fuel jet with a resolution of 0.3 mm, while the grid is stretched by a factor of 1.12 from the pilot towards the lateral boundaries. The mean axial velocities at the inflow for the fuel, jet and pilot are set to power-law profiles with exponents 1/6

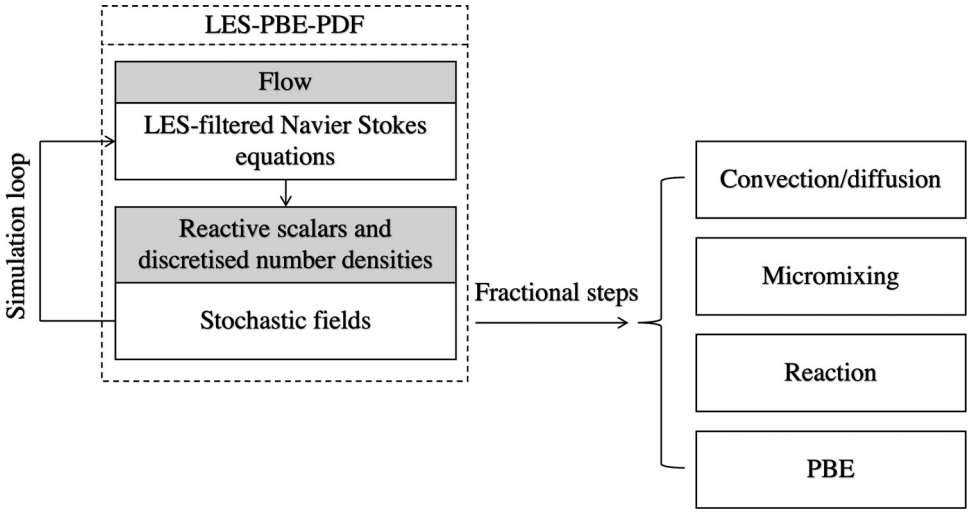


Fig. 1. An overview of the LES-PBE-PDF code implementation.

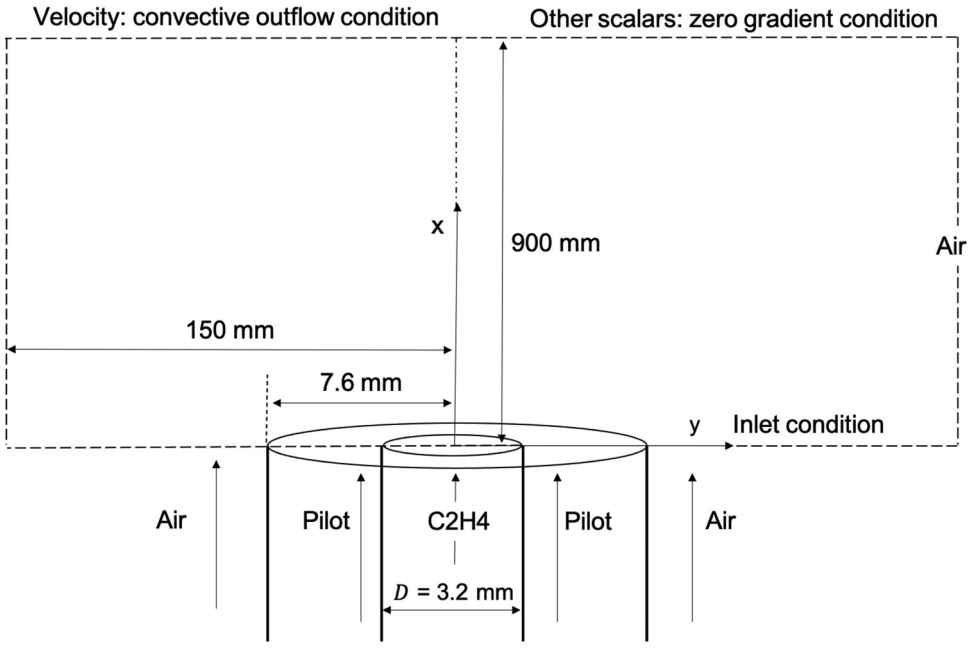


Fig. 2. Illustration of the burner and computational domain.

and 1/2, respectively. On the contrary, the air co-flow is set to a constant mean axial inflow velocity. The turbulence intensities for all flows are set to 6%. The RMS inflow velocity for the fuel jet varies quadratically (at the jet rim it is four times as large as the nominal centreline value) and maintains a constant value for the pilot and co-flow. The initial composition of the pilot is the adiabatic equilibrium one for the premixed mixture. The four lateral boundaries are set to have the same composition and velocity as the co-flow air, and entrainment/outflow is allowed at the lateral boundaries. At the domain exit, the convective outflow condition is applied to the velocity field and the zero gradient condition is applied to the scalar fields. A schematic illustration of the computational domain is given in Fig. 2.

Studies of convergence of the stochastic field method have shown that eight fields are sufficient to obtain convergence for the means and RMS of the scalars. Mustata et al. [86] used eight and sixteen stochastic fields for a turbulent diffusion flame but found that the changes in the mean and RMS of the major scalars were very small, and a similar conclusion was reached by Jones and Navarro-Martinez [87]. In accordance with these findings, eight fields are employed in our simulations.

As velocity measurements are not available, we adopt a simplified inflow geometry where the thin wall of the tube and the jet immersion are ignored. A similar configuration was used by Sewerin and Rigopoulos [27], where good agreements for both mean and RMS velocity profiles were achieved for the Delft III turbulent flame. The temporal statistics have been collected for a period of 0.15 s (time step $\Delta t = 3 \times 10^{-6}$ s), corresponding to about three flow-through times and starting after the simulation had reached a statistically steady state, which was sufficient for them to become time-invariant.

6. Results and discussion

6.1. Comparison with experimental data

In order to validate the LES-PBE-PDF approach, the numerical results will be compared to the measurements in the Sandia ethy-

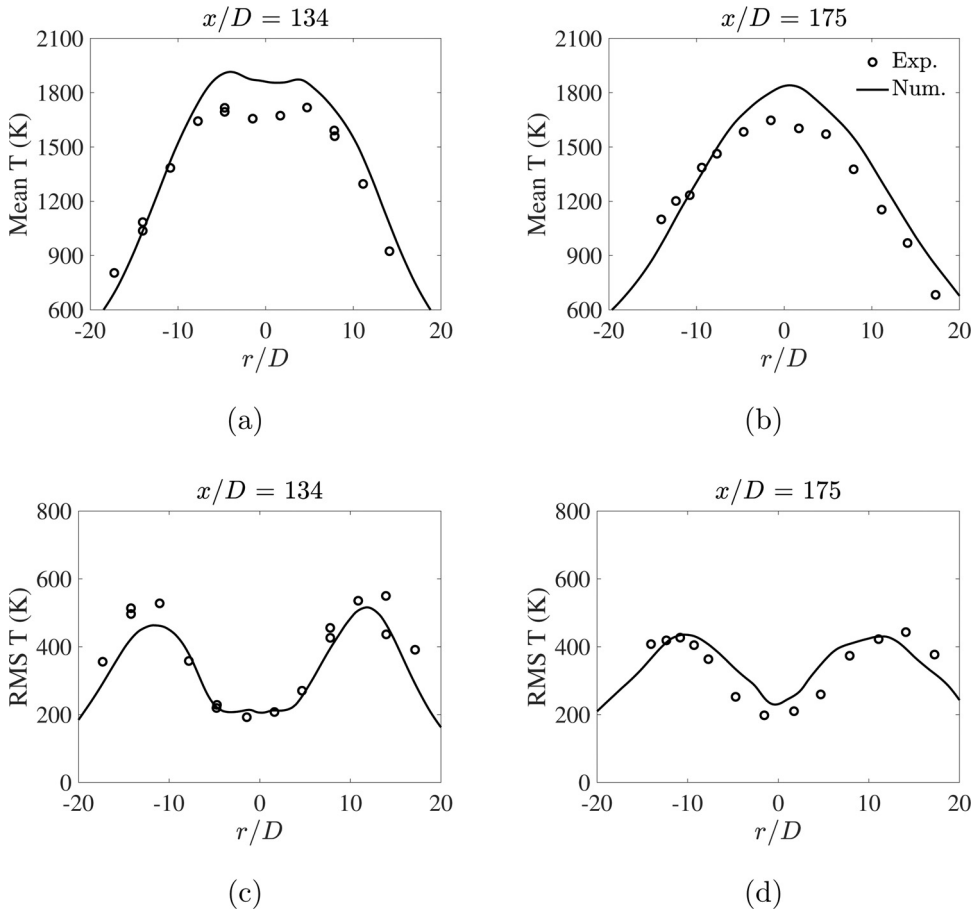


Fig. 3. Comparison of mean and RMS temperature radial profiles between experimental data (symbols) and numerical results (line) at $x/D = 134$ and $x/D = 175$.

lene flame. The following experimental data are available for comparison:

- CARS temperature and X_{O_2}/X_{N_2} [88]
- PLIF OH and PLIF PAH [89]
- Axial profile of soot intermittency [89]
- LII soot volume fraction [90]

Figure 3 shows a comparison of computed radial mean and RMS temperature profiles with experimental results at $x/D = 134$ and $x/D = 175$ [88], while Fig. 4 shows a comparison of radial mean and RMS X_{O_2}/X_{N_2} profiles at the same heights. Overall, the predictions are reasonably good for both mean and RMS values. At $x/D = 134$, an overestimation of the mean temperature around the centreline is observed (Fig. 3a) and the mean mole fraction ratio X_{O_2}/X_{N_2} (Fig. 4a) is slightly underpredicted, while the peaks of the RMS temperature (Fig. 3c) and RMS X_{O_2}/X_{N_2} (Fig. 4c) radial profiles from the simulation are in very good agreement with the experimental data. A similar level of discrepancy was also featured in the simulation of the same flame by Rodrigues et al. [28] which featured a much finer grid (an unstructured grid with about 10M cells/1.7M nodes with a typical cell size of 0.2 mm at the jet exit). At $x/D = 175$, an overestimation of the mean temperature profile at the centreline (Fig. 3b) is also observed, while the mean X_{O_2}/X_{N_2} profile (Fig. 4b) is slightly overpredicted. However, the shape of the flame tip is well reproduced and the RMS tempereture (Fig. 3d) and X_{O_2}/X_{N_2} (Fig. 4d) radial profiles are in good agreement with the experimental data. The underprediction of the temperature is probably associated with the underprediction in soot volume fraction that will be discussed below.

Figure 5 shows a comparison of simulation results and measurements for the mean OH radial profiles at different heights. As the experimental measurements are PLIF signals rather than mole fractions, numerical and experimental results are normalised by their corresponding maximum values for each height. Very good agreement is observed, apart from some small discrepancies at $x/D = 117.2$ and $x/D = 132.8$. This result indicates a satisfactory prediction of the mean flame shape. Fig. 6 shows a comparison of mean PAH radial profiles at different heights between numerical results and experimental measurements [89]. Note that C_10H_8 (A_2) is chosen as the representative PAH species in the numerical results, as its mass fraction is dominant compared to that of other PAHs contributing to soot nucleation/condensation. Despite a wider PAH profile at the lower region of the flame, as indicated in Fig. 6, the overall agreement is also satisfactory. As will be discussed later and shown in Fig. 14, the nucleation/condensation in the early region ($x/D = 54.7$) is not as significant as that in the peak region ($x/D = 85.9$). Consequently, the discrepancy at $x/D = 54.7$ is not expected to result in a significant discrepancy in the predictions. Good matches in these profiles are required for a proper account of soot oxidation, nucleation/condensation and even surface growth as OH initialises H-abstraction in the HACA mechanism.

The axial profiles of mean and RMS soot volume fraction along the centreline are shown in Fig. 7. While qualitative features such as the locations of the soot formation zone and peak values are predicted well, the magnitudes are considerably underpredicted. In the literature, an overestimation of soot volume fraction by a factor of 2 [28] for the same turbulent jet flame can be found, whereas a level of underprediction similar to our work was also observed in several studies [10,31]. In particular, several cases were

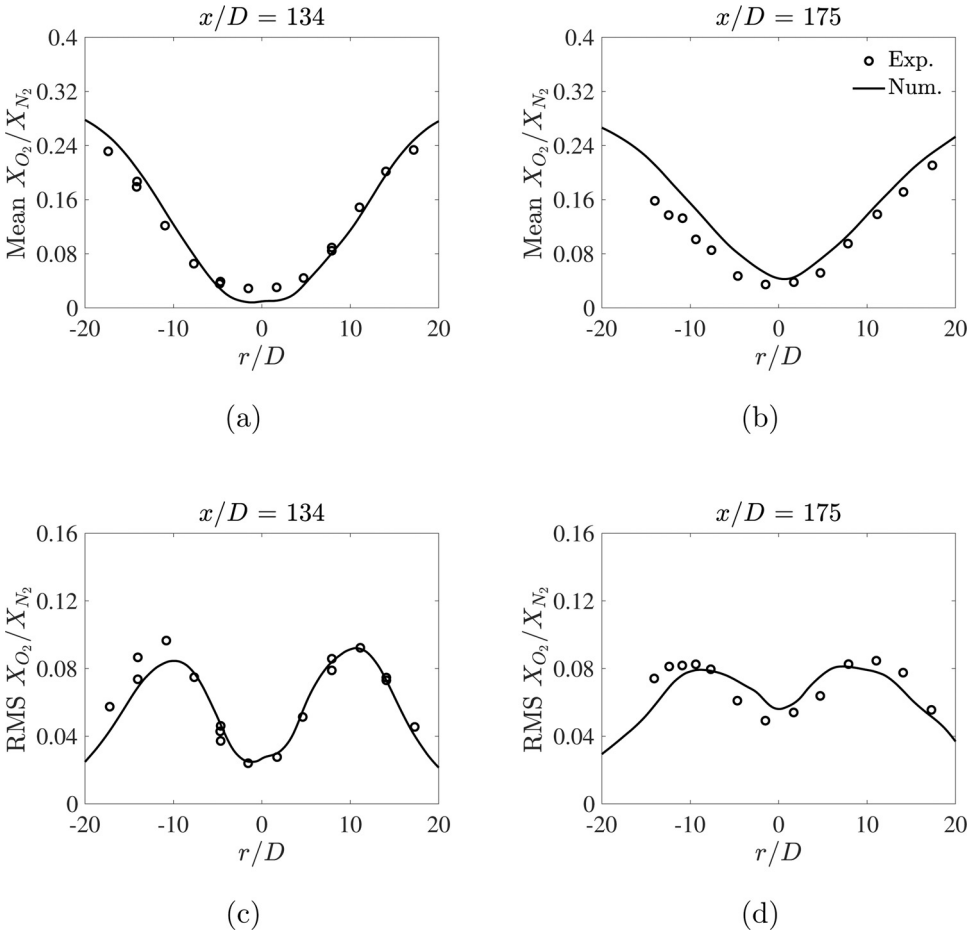


Fig. 4. Comparison of mean and RMS X_{O_2}/X_{N_2} radial profiles between experiment data (symbol) and numerical results (line) at $x/D = 134$ and $x/D = 175$.

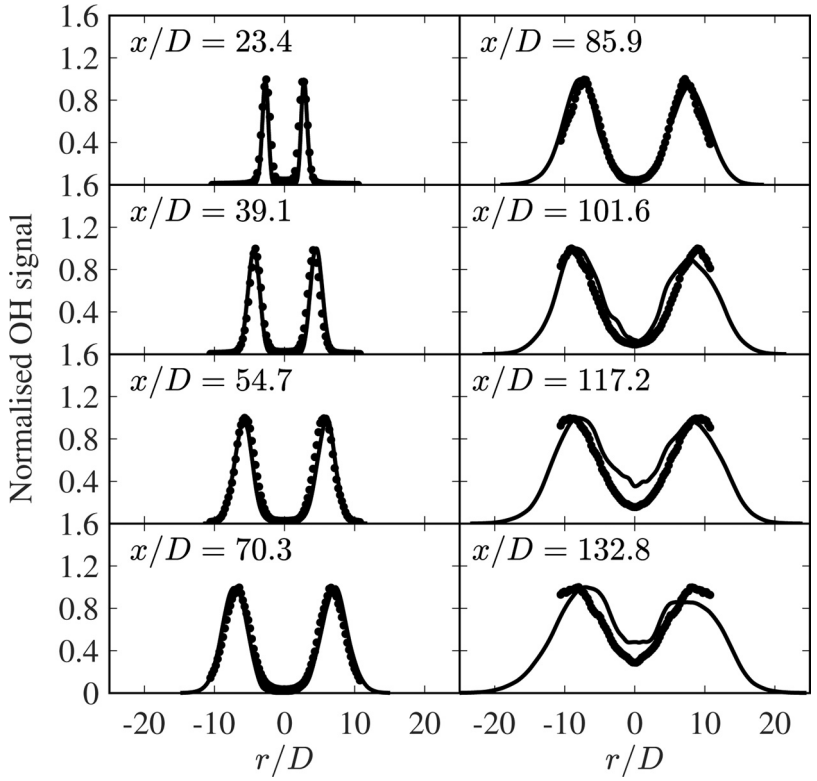


Fig. 5. Radial profiles of normalised mean OH mass fraction from simulations (black line) and normalised OH signals from experimental data (black symbols).

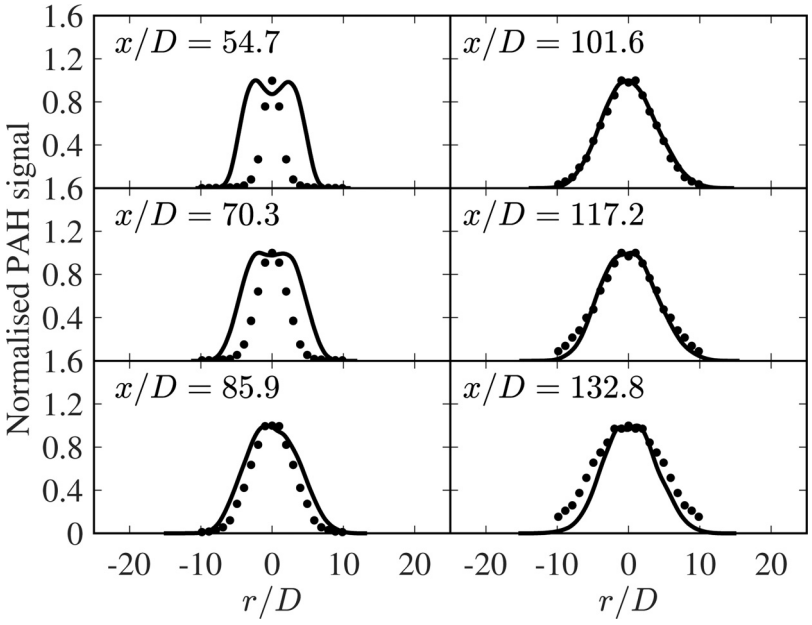


Fig. 6. Radial profiles of normalised mean A_2 mass fraction from simulations (black line) and normalised PAH signals from experimental data (black symbols).

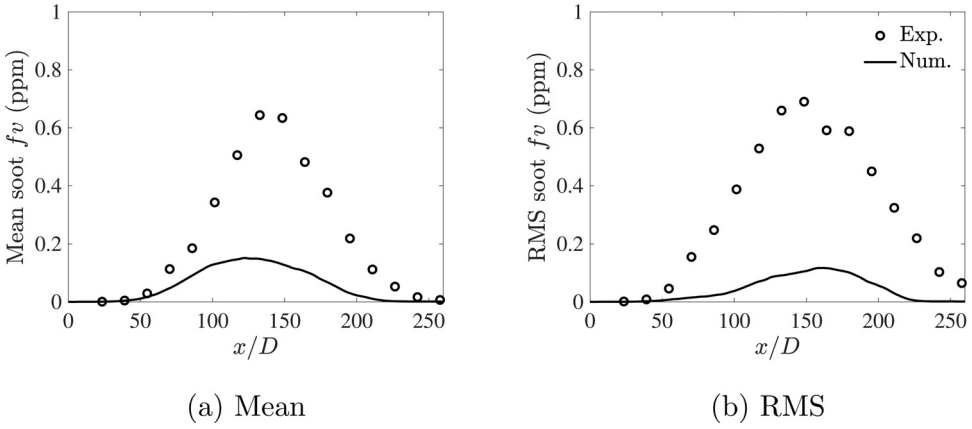


Fig. 7. Axial profiles of the mean and RMS soot volume fraction along the flame centreline.

conducted in Ref. [32] with different mixture fraction parameters associated with the conditional soot subfilter PDF model, and in some of these cases an underprediction by an order of magnitude were obtained, while in one case an overprediction by a factor of 3 was observed. In that work, the presumed PDF method of Mueller and Pitsch [19] was augmented by introducing a mixture fraction dependence on the soot subfilter PDF model and an additional variable, and results were shown for different values of that variable. Such a modification cannot be introduced to transported PDF methods in a straightforward way, however, because in that case the micromixing frequency is the only parameter of the subgrid model. As mentioned in Section 2.4, a mechanistic augmentation of the micromixing model to account for differential diffusion of soot and gas-phase species is not attempted in the present work, where the standard form of the IEM model is employed.

Furthermore, Fig. 8 compares radial profiles of mean soot volume fraction at different heights. The location and qualitative trends in the experimental data are reproduced, but the magnitude of soot volume fraction in the region away from the jet is underpredicted. Moreover, Fig. 9 compares the normalised RMS radial profiles of soot volume fraction for the same heights, and similar features as for the means values are observed. The good predictions of the position and the shape of the profiles indicate that several elements of the model, are performing well, but a quantitative agreement is still not possible. It must be mentioned that, in our simulation of the laminar Santoro flame with the same kinetics [67], while the integrated soot volume fraction at different heights above burner was predicted reasonably well (with an underprediction to a smaller extent), the centreline profile was underpredicted to an extent similar to the one observed in the present study. Measurements of integrated soot volume fraction similar to those in the Santoro flame are not available for the turbulent Sandia ethylene flame.

In addition, Fig. 10 shows a comparison of predicted and measured soot intermittency along the flame centreline. The resolved soot intermittency at each spatial position is defined experimentally as the probability of observing an instantaneous value of soot volume fraction lower than 0.03 ppm [89]. The simulation results seem to be translated upstream with an underestimation in the region between $x/D = 60$ and $x/D = 120$. The low intermittency

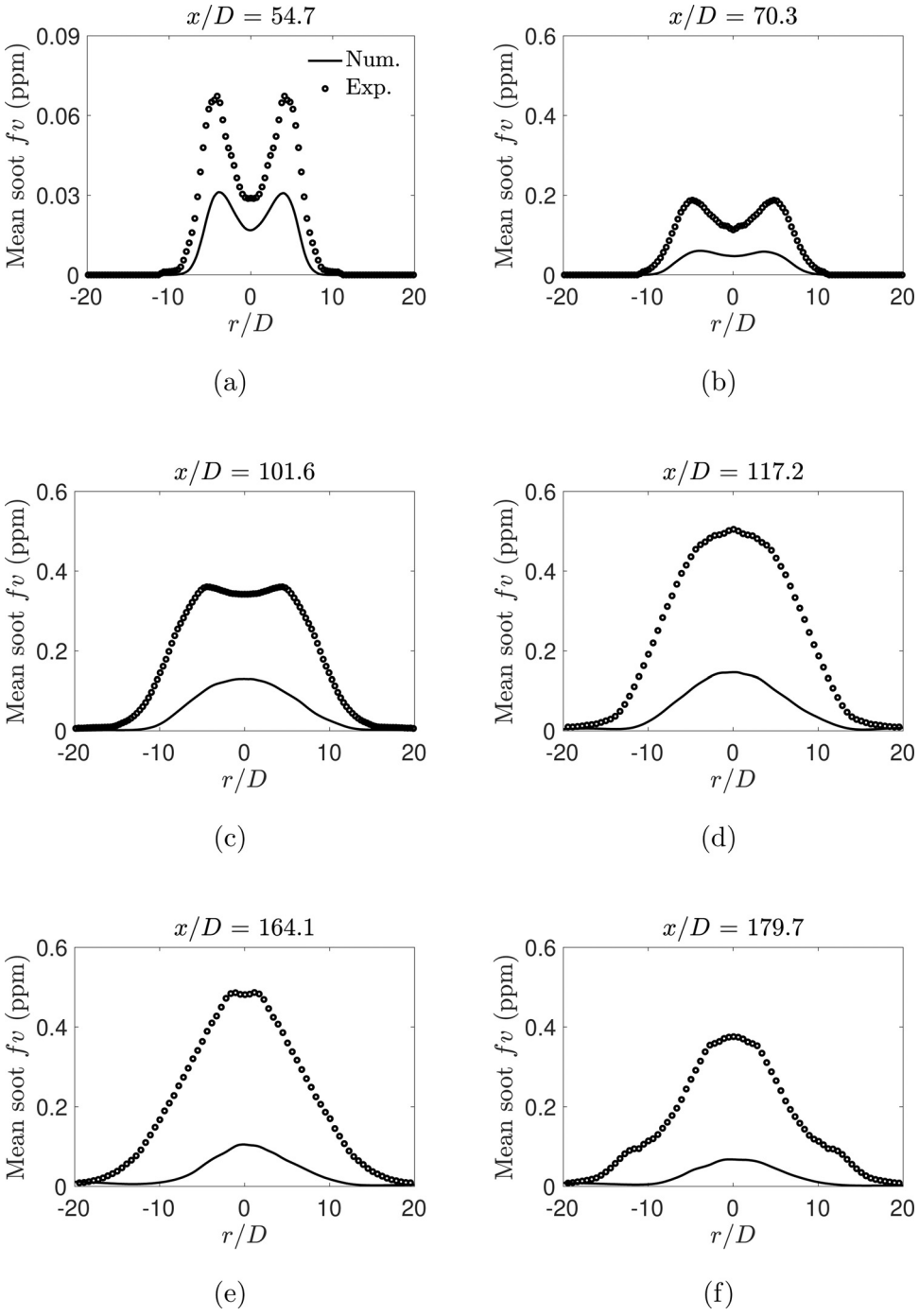


Fig. 8. Predictions of the mean soot volume fraction radial profiles at different heights.

around $x/D = 100$ is caused by the combined impact of both nucleation/condensation and surface growth. We can see in Fig. 14a that, in the region $x/D = 80$ to $x/D = 140$, nucleation/condensation decrease but surface growth increases. The level of net mass addition is still high (as shown by the dashed line in Fig. 14a). Since the intermittency is defined as the possibility of finding particles below 0.03 ppm, a high level of mass addition would lead to soot particles larger than 0.03 ppm, thus leading to lower intermittency.

In summary, despite some discrepancies in the simulation compared to the experiment, the overall performance of the proposed LES-PBE-PDF approach is reasonable in light of the current state of the art in the modelling of turbulent sooting flames. As the aim of this simulation was to use the same kinetics as in the simulation of the Santoro flame [67], there was no space for improving the results via parameter adjustment. The level of agreement obtained does indicate that several elements in the modelling approach are performing well, but it is still not possible to obtain quantitative agreement. An analysis of the sources of uncertainty is presented in the following section.

6.2. Discussion of modelling uncertainties

At present, it is not possible to determine conclusively the reasons for the remaining discrepancies, the most important of which is the underprediction of the soot volume fraction. Some light,

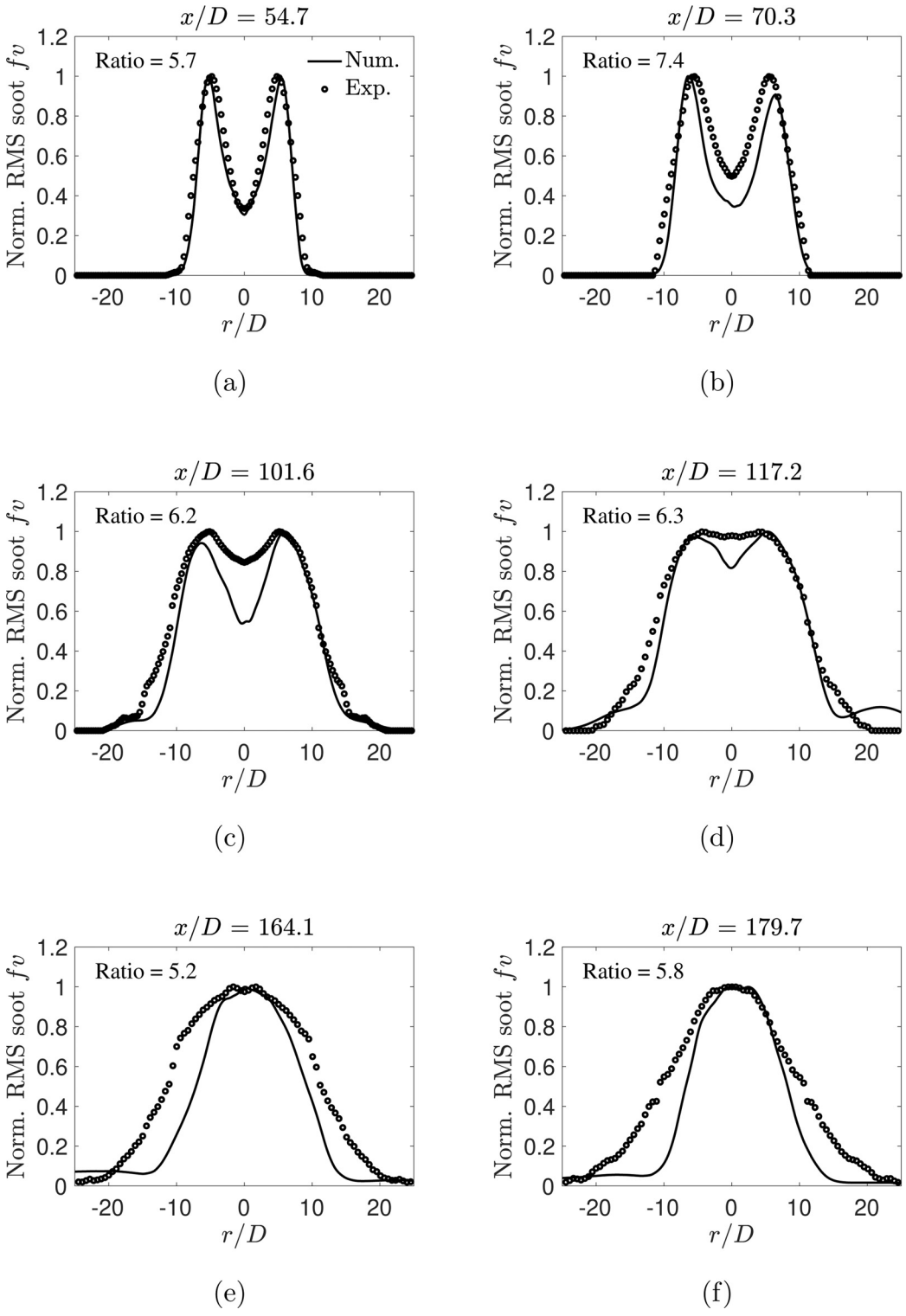


Fig. 9. Predictions of the normalised RMS soot volume fraction radial profiles at different heights. The RMS is normalised by the associated maximum mean soot volume fraction. The ratio shown indicates the maximum experimental value over the maximum predicted one at each height.

however, can be shed by considering the validation of various elements of our approach in previous works. As mentioned before, the kinetic parameters in the present study were chosen to be the same as in our previous simulation of the laminar Santoro flame [67], while the LES parameters are the same as in a previous simulation of a jet sooting flame by our group [27] carried out with the same code.

LES has been shown to provide an accurate description of the fluid dynamics of jet flames away from walls [69]. In our previous turbulent sooting flame simulation [27], the predicted flow field was validated with experimental measurements and good agreement was obtained. While the validation dataset in the present study does not provide flow field measurements, some inferences about the accuracy of the flow field prediction may be made from

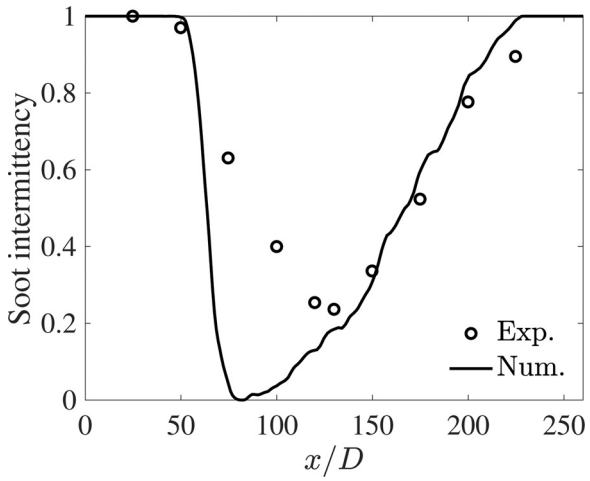


Fig. 10. Comparison of numerical and experimental results for the axial soot intermittency profile along the flame centreline.

the computed scalar fields. The temperature and species profiles are well predicted apart from an underprediction of the peak temperature, which was also present in the best so far simulation of the flame studied here [28] featuring a much finer grid than the present study, and which is most likely to do with soot volume fraction and kinetics rather than fluid dynamics. The spread of the means and RMS of most quantities is also well predicted and generally the qualitative features of soot distribution are reproduced, while the main discrepancy is in the soot volume fraction, which is also present in all other studies of this flame. These features suggest that the flow field is simulated to a good accuracy.

The solution of the population balance with the conservative sectional method contains no modelling assumptions and has been shown to be accurate when validated with analytical and similarity solutions [65,67]. The convergence of the stochastic fields method has also been investigated [86,87] and the number of fields employed here has been shown to be sufficient.

With respect to turbulence-chemistry interaction, micromixing is the most important unclosed term in the transported PDF approach. While a uncertainty about the micromixing model remains, its impact is diminished in LES as compared with RANS and simulations of turbulent jet flames of the Sandia type with LES-PDF and stochastic fields have shown that concentration profiles can be predicted quite well, except for cases with excessive local extinction [69]. The impact of the micromixing model on soot is more questionable, however, due to the very low diffusivity of soot that differs greatly from that of gas-phase species. While this difference in diffusivities could be accommodated at the grid level, the IEM model does not distinguish between species and soot and this is something that should be investigated in future research, possibly via the development of a micromixing model particularly for soot. Attili et al. [14] investigated the impact of non-unity Lewis number in turbulent nonpremixed sooting flame and concluded that the impacts on flow field and major species such as OH and C_2H_2 was not significant, but a relatively large difference was observed in the field of A_2. Furthermore, naphthalene is very sensitive to turbulent mixing (see e.g. [7,12]).

While micromixing is a modelling uncertainty that should be investigated in future research, it must be noted that the underprediction in soot volume fraction along the centreline was also present in our laminar Santoro flame simulation [67], where the issue of micromixing modelling were not present. Therefore, kinetics and particularly surface reactivity remain a major sources of uncertainty. More importantly, the model employed for surface reactivity is relatively simple and accounts for the change of temperature only. Future work may consider incorporating models that consider the effect of soot carbonisation on surface reactivity [91,92] as well as aerosol dynamics models that account for the evolution of aggregate structure in a more realistic way and include a timescale associated with the fusion of primary particles [67]. Further combined laminar and turbulent flame studies are also needed to determine the extent to which each of the kinetic processes contributes to the discrepancy in the volume fraction prediction.

6.3. Investigation of soot formation

In this section, the soot formation processes in the turbulent flame are further analysed. Fig. 11 shows contour plots of the instantaneous temperature, soot volume fraction and soot number density. As indicated in Fig. 11b,c, soot is restricted to fuel-rich regions within the mixture fraction isocontour. Most soot particles are located in the region between $x/D = 40$ and $x/D = 100$, while the soot volume fraction peaks at a region between $x/D = 80$ and $x/D = 160$, consistent with the prediction in Fig. 7 and experimental observations [89]. Similar patterns were observed also in other simulations [10,28]. The distinct separation of the peak zones in these two plots indicates that soot would experience a strong mass addition after being formed, which is confirmed below (Fig. 13c).

To further analyse the soot formation phenomena associated with the N and f_v fields, the instantaneous and mean contour plots of mole fraction of several key species are shown in Fig. 12, while Fig. 13 shows the instantaneous and mean soot volume fraction contribution rates from nucleation, condensation, surface growth and oxidation. Regarding PAHs, only the contour plot of A_2 mole fraction is shown, because the concentration of A_2 is orders of magnitude larger than that of other PAHs contributing to dimer formation; furthermore, only the oxidation rate due to OH is shown, as it is much larger than the one due to O_2 (as shown in Fig. 14, to be discussed later). Firstly, by comparing Fig. 12a with Fig. 11c, it is clear that A_2 is formed before the appearance of measurable soot in the flame and is limited to the inner jet, consistent with the experimental observation in Ref. [89]. Fig. 13a,b and Fig. 12a show a strong spatial correlation between nucleation, condensation and A_2 species. This feature is expected, as the nucleation and condensation depend on the dimer concentration, which is associated with the concentration of A_2. Fig. 13a also confirms the early nucleation indicated by Fig. 11b. By comparing Fig. 13a,b with c, it can be seen that surface growth is responsible for most of the mass addition, as its contribution rate is one order of magnitude larger than that of condensation. According to Ref. [89], the structure of OH should develop from straight, thin layers at the jet exit to increasingly wrinkled, thick structures downstream from the nozzle, which is well reproduced in Fig. 12c. A weak spatial correlation between growth rate and C_2H_2 is observed. As discussed in Ref. [67], this is because the rate-limiting reactions in the current soot kinetics are the hydrogen abstraction reactions, which means that radical species (e.g., H and OH) contribute more to surface growth than C_2H_2. In the regions that are rich in OH and H, C_2H_2 is consumed via the acetylene addition reaction step in HACA mechanism, which can be observed in Fig. 12b-d. These observations are consistent with those reported in Ref. [28] in a simulation of the same flame.

Figure 14 shows several features of soot formation along the centreline, as predicted by the LES-PBE-PDF method. Similar to the observation in Fig. 13, a spatial correlation between the mean nucleation and condensation can be found, and the mass addition along the centreline is dominated by the nucleation and condensation in the early region and by surface growth afterwards, leading to a separation of the locations of peak values in the soot number

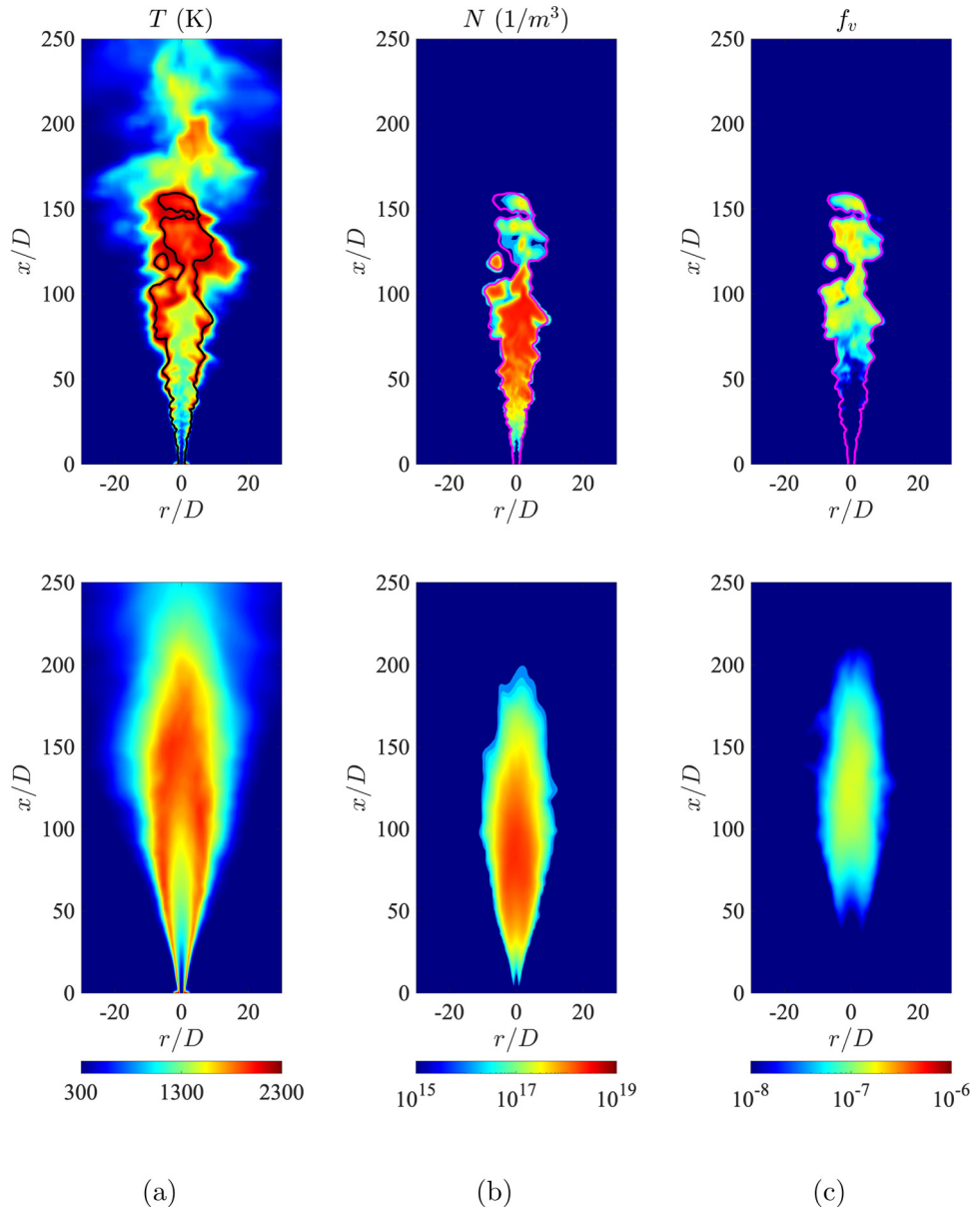


Fig. 11. Contour plots of instantaneous (top) and mean (bottom) (a) temperature, (b) soot number density and (c) soot volume fraction computed from the LES-PBE-PDF model. The isocontour of stoichiometric mixture fraction ($Z = 0.0634$) is shown as a solid line in the instantaneous contour plot (black in (a) and magenta in (b) and (c)).

density and volume fraction profiles. The mean primary particle diameter increases with distance from the nozzle up to the point where the oxidation process dominates. A similar trend was also observed experimentally by Boyette et al. [93]. As the oxidation due to OH is much larger than the one due to O_2, the prediction of the soot volume fraction along the centreline is mostly controlled by surface growth and OH oxidation. Since the rate-limiting process in HACA mechanism is the H-abstraction step (which involves H and OH radicals), as discussed in [67,92], a good prediction of OH is important for the surface growth process.

Figure 15 shows the instantaneous particle size distribution at three different axial cross-sections. At $x/D = 70.3$ the process is nucleation/condensation dominated, at $x/D = 132.8$ it is dominated by surface growth while at $x/D = 210.9$ it is dominated mostly by oxidation. Note that the points in which the soot volume fraction is below 0.001 ppm have been filtered out. At these three locations, the highest soot number density appears for particles below 2 nm (Fig. 15a), which is in accordance with the experimental observation in [94]. Fig. 15b shows the particle size distribution function (PSDF) defined as $PSDF(d) = (1/N_t')dN'/dlogD$ [95], where N_t' is the total local particle number [95]). In the early region where the flame is less intermittent, the PSDFs have a unimodal shape, which is flattening as we move towards the flame front and the number of larger aggregates increases. Both unimodal and bimodal shapes of the PSDF can be seen in the surface growth-dominated region. As discussed also in [95], soot particles going through different trajectories undergo different sooting processes. The combined effects of surface growth, oxidation, coagulation and nucleation/condensation lead to a bimodal PSDF which becomes more complex away from the jet nozzle. However, in the region far away from the jet, the PSDF assumes a unimodal shape due to strong oxidation. Fig. 15c shows the normalised soot volume fraction distribution. At all three locations, the majority of soot volume comes from aggregates larger than 10 nm, while the peak of the distribution shifts towards a larger size as the residence time of aggregates increase, from 10 to 30 nm at $x/D = 70.3$ to 30–50 nm

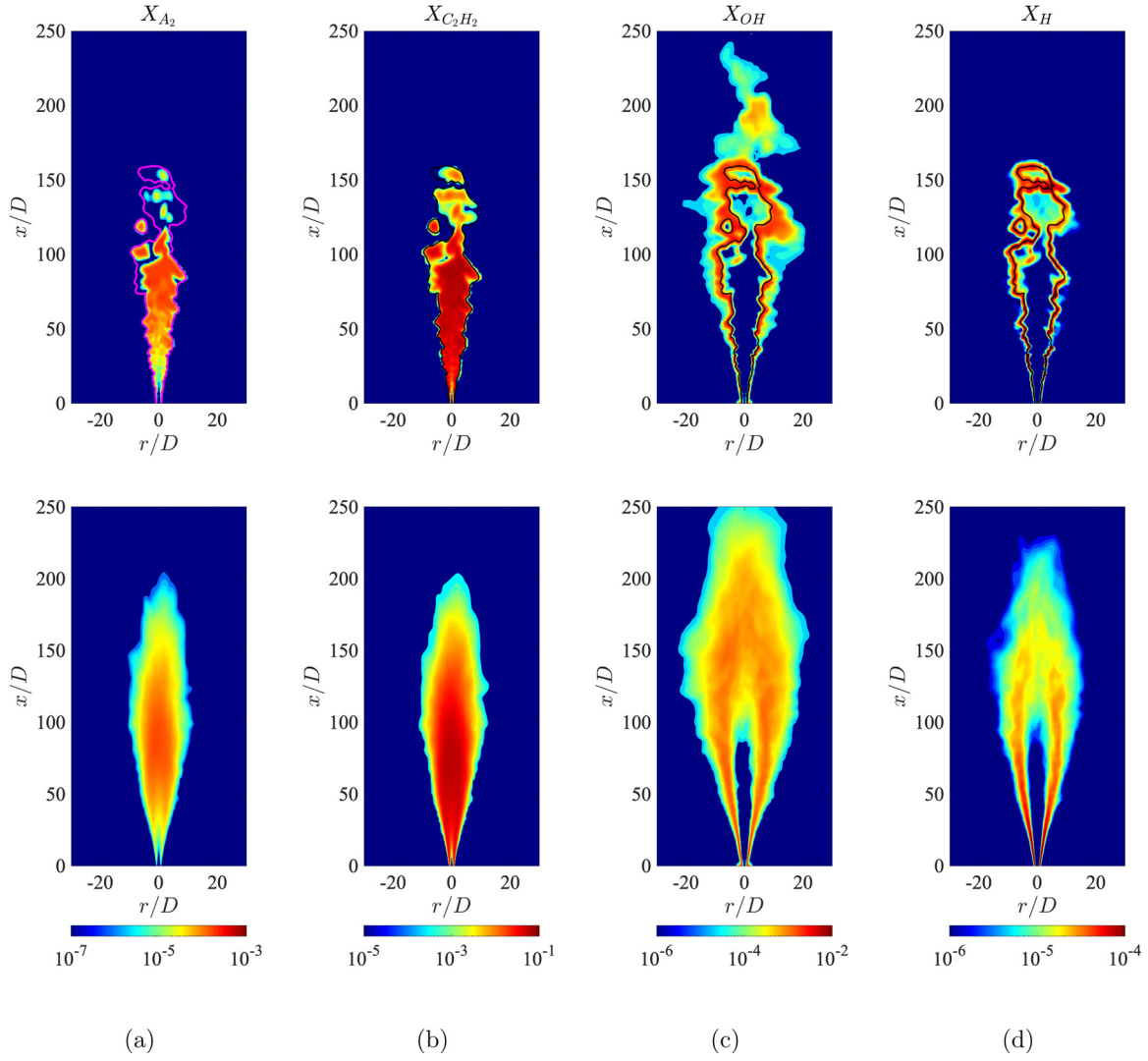


Fig. 12. Contour plots of the instantaneous (top) and mean (bottom) (a) A_2 mole fraction, (b) C_2H_2 mole fraction, (c) OH mole fraction and (d) H mole fraction computed from the LES-PBE-PDF model. The isocontour of stoichiometric mixture fraction is shown in solid line in the instantaneous contour plot (magenta in (a), and magenta in the rest plots).

Table 1
Average runtimes for the LES-PBE-PDF method to advance one time step ($\Delta t = 3 \times 10^{-6}$ s) on 20 nodes (480 MPI processes) of ARCHER supercomputer.

Process	Average runtime (s)	Percentage
Scalar convection/diffusion	3.67	12.25%
Micromixing	1.59	5.31%
Gas phase reaction	14.86	49.60%
PBE solution	5.33	17.79%
Flow field	0.42	1.40%
All other processes	4.09	13.65%
Total CPU cost	29.96	-

at $x/D = 132.8$. At $x/D = 210.9$, the size corresponding to the peak experiences less fluctuation, from 30 to 40 nm.

6.4. Analysis of computational performance

Table 1 shows the CPU breakdown for each process in the simulation, calculated based on an average over 3000 time steps. It is evident that the greatest CPU cost is due to the gas-phase reaction, which takes almost half of the total CPU time. The solution of the PBE with the sectional method requires 17.79% of the total CPU time. The sectional method requires also the transport of 60 scalars in addition to the 149 species and the flow field variables, hence approximately one fourth of the transport and micromixing time should be attributed to it, but overall the computational overhead incurred by it is less than 25%, indicating that it is not a major overload in the LES-PBE-PDF simulation. It must also be mentioned that the chemistry was accelerated by approximately one order of magnitude with various ways mentioned in Section 4 which do not incur any loss of accuracy, such as hard-coding the mechanism.

The integration of chemical kinetics therefore remains the bottleneck in the simulation of sooting flames with the LES-PBE-PDF method. In future work, this can be alleviated by using mechanism reduction and tabulation methods. The In-Situ Adaptive Tabulation (ISAT) method [96] has traditionally been employed to accelerate chemistry in PDF methods. Another method that can be used in this context is Hybrid Transported-Tabulated Chemistry (HTTC), originally developed for premixed combustion [97] and later extended to partially premixed combustion [98]. Machine learning tabulation methods have also been used recently with success in turbulent non-premixed jet flames similar to the one employed in the present study [99–101]. Recent efforts have also employed

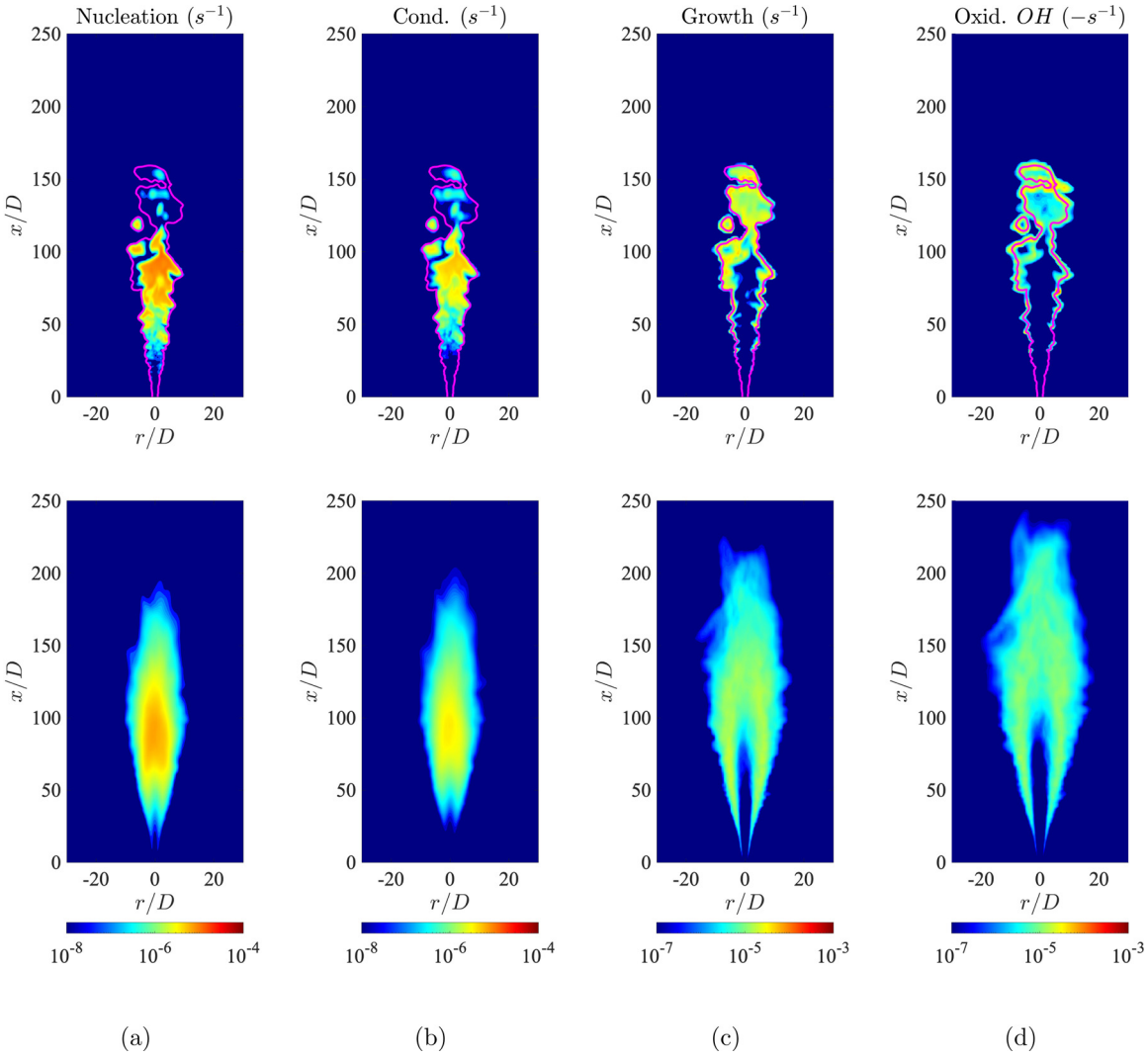


Fig. 13. Contour plots of the instantaneous (top) and mean (bottom) (a) nucleation rate, (b) condensation rate, (c) growth rate, and (d) oxidation rate due to OH computed from the LES-PBE-PDF model. The isocontour of stoichiometric mixture fraction is shown in solid magenta line in the instantaneous contour plot.

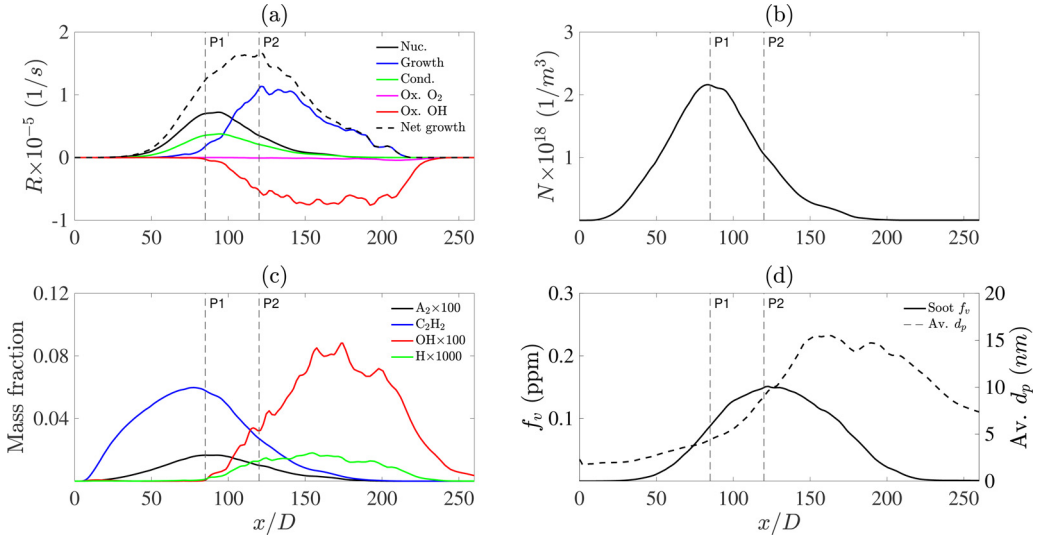


Fig. 14. Mean profiles of (a) soot volume fraction contribution rate due to each soot formation process, (b) particle number density, (c) mass fraction of key species, and (d) soot volume fraction and mean primary particle diameter along the centreline, as predicted by the LES-PBE-PDF method. P1 and P2 indicate the locations of the peak values in the soot number density and volume fraction profiles respectively.

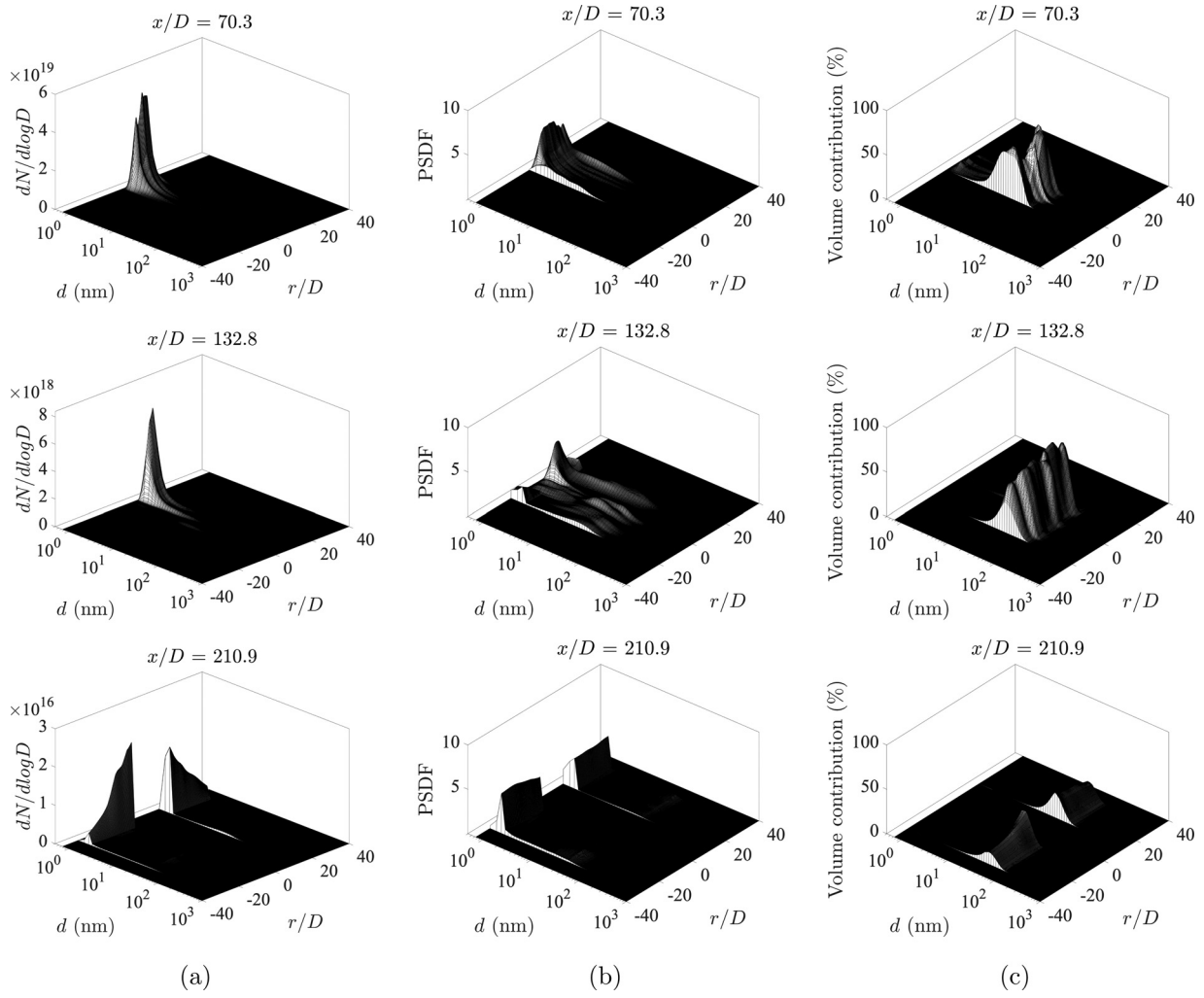


Fig. 15. Instantaneous soot (a) particle size distribution, (b) particle size distribution function, and (c) normalised soot volume distribution at three axial cross-sections computed from the LES-PBE-PDF model.

machine learning for the solution of the PBE in laminar premixed sooting flames [102].

7. Conclusions

The present paper had two main aims. The first one was to present an LES-PBE-PDF approach to soot modelling that includes detailed kinetics and comprehensive models for all aerosol dynamics processes, compare its results with experiments and examine its computational performance and feasibility. The second one was to simulate a turbulent diffusion flame using the same models and parameters for gas-phase chemistry, soot kinetics and aerosol dynamics as those employed in a previous work [67] for a simulation of the Santoro laminar diffusion flame.

In the methodology presented here, the PBE-PDF method accounts for the source terms associated with turbulence-chemistry and turbulence-soot interactions without the need for closure assumptions, as they appear in closed form, but requires a model is required for the micromixing term. While the lower diffusivity of soot can be accommodated at the grid level, the sub-grid mixing is modelled via the augmented IEM micromixing model which employs a single micromixing frequency for all scalars. In line with the approach adopted in this paper to employ the models without modifications of parameters, no modification in the micromixing frequency was attempted, but this is an element of the approach that should be reconsidered in future work via the development of an improved micromixing model for soot. A comprehensive mechanism of combustion and PAH formation is employed to support a detailed soot aerosol dynamics model based on a population balance equation which is solved via a conservative sectional method. Finally, the stochastic fields method is employed for solving the LES-PBE-PDF equations.

In the application to the Sandia turbulent non-premixed sooting flame, overall reasonably good agreement was obtained for the mean and RMS profiles of temperature, RMS X_{O_2}/X_{N_2} and normalised species profiles. The location and qualitative shape of the soot volume fraction axial and radial profiles were also well predicted, but the soot volume fraction was underpredicted. By examining the elements of the methodology and the degree to which they have been validated in previous studies, the most likely sources of this discrepancy were identified to be the micromixing model and the kinetics employed. It is clear that further research is needed to reach the state where quantitative agreement in simulations of turbulent sooting flames can be accomplished without adjustments, but the fact that several features of the soot formation could be captured with the same kinetic and aerosol dynamic models employed in both the laminar and turbulent flame is encouraging. Apart from the improvements in the modelling of micromixing (as mentioned above), future work could consider incorporating kinetics that account for the effect of soot carbonisation

on surface reactivity and population balance models that provide a more detailed account of the evolution of aggregate structure. Finally, the distribution of the CPU time among the various elements of the method showed that the incorporation of the PBE with the conservative sectional method into LES-PDF methods is feasible, as the CPU time required for the transport of the extra scalars and solution of the PBE was less than 25% of the total CPU time.

Declaration of Competing Interest

The authors declare that they have no known competing financial interests or personal relationships that could have appeared to influence the work reported in this paper.

Acknowledgments

Binxuan Sun gratefully acknowledges the financial support of the Imperial-CSC scholarship scheme. The authors also wish to acknowledge the use of the following HPC facilities: Imperial College Research Computing Service (DOI: 10.14469/hpc/2232), ARCHER UK National Supercomputing Service (http://www.archer.ac.uk) via the UK Consortium on Turbulent Reacting Flows (www.ukctrf.com) supported by EPSRC grant EP/R029369/1 and UK Materials and Molecular Modelling Hub partially funded by EPSRC (EP/P020194/1 and EP/T022213/1).

References

[1] K. Donaldson, L. Tran, L.A. Jimenez, R. Duffin, D.E. Newby, N. Mills, W. MacNee, V. Stone, Combustion-derived nanoparticles: a review of their toxicology following inhalation exposure, Part. Fibre Toxicol. 2 (2005) 10.
[2] G.A. Kelesidis, E. Goudeli, S.E. Pratsinis, Flame synthesis of functional nanostructured materials and devices: surface growth and aggregation, Proc. Combust. Inst. 36 (1) (2017) 29–50.
[3] S. Rigopoulos, Population balance modelling of polydispersed particles in reactive flows, Prog. Energy Combust. Sci. 36 (4) (2010) 412–443.
[4] V. Raman, R.O. Fox, Modeling of fine-particle formation in turbulent flames, Annu. Rev. Fluid Mech. 48 (2016) 159–190.
[5] S. Rigopoulos, Modelling of soot aerosol dynamics in turbulent flow, Flow Turbul. Combust. 103 (3) (2019) 565–604, doi:10.1007/s10494-019-00054-8.
[6] H. Wang, Formation of nascent soot and other condensed-phase materials in flames, Proc. Combust. Inst. 33 (1) (2011) 41–67.
[7] F. Bisetti, G. Blanquart, M.E. Mueller, H. Pitsch, On the formation and early evolution of soot in turbulent nonpremixed flames, Combust. Flame 159 (1) (2012) 317–335.
[8] F. Bisetti, A. Attili, H. Pitsch, Advancing predictive models for particulate formation in turbulent flames via massively parallel direct numerical simulations, Philos. Trans. R. Soc. A 372 (2022) (2014) 20130324.
[9] M.E. Mueller, V. Raman, Effects of turbulent combustion modeling errors on soot evolution in a turbulent nonpremixed jet flame, Combust. Flame 161 (7) (2014) 1842–1848.
[10] Y. Xuan, G. Blanquart, Effects of aromatic chemistry-turbulence interactions on soot formation in a turbulent non-premixed flame, Proc. Combust. Inst. 35 (2) (2015) 1911–1919.
[11] A. Attili, F. Bisetti, Application of a robust and efficient Lagrangian particle scheme to soot transport in turbulent flames, Comput. Fluids 84 (2013) 164–175.
[12] A. Attili, F. Bisetti, M.E. Mueller, H. Pitsch, Formation, growth, and transport of soot in a three-dimensional turbulent non-premixed jet flame, Combust. Flame 161 (7) (2014) 1849–1865.
[13] A. Attili, F. Bisetti, M.E. Mueller, H. Pitsch, Damköhler number effects on soot formation and growth in turbulent nonpremixed flames, Proc. Combust. Inst. 35 (2) (2015) 1215–1223.
[14] A. Attili, F. Bisetti, M.E. Mueller, H. Pitsch, Effects of non-unity Lewis number of gas-phase species in turbulent nonpremixed sooting flames, Combust. Flame 166 (2016) 192–202.
[15] A. Wick, A. Attili, F. Bisetti, H. Pitsch, DNS-driven analysis of the flamelet/progress variable model assumptions on soot inception, growth, and oxidation in turbulent flames, Combust. Flame 214 (2020) 437–449.
[16] A. Wick, M. Frenklach, H. Pitsch, Systematic assessment of the method of moments with interpolative closure and guidelines for its application to soot particle dynamics in laminar and turbulent flames, Combust. Flame 214 (2020) 450–463.
[17] H. El-Asrag, T. Lu, C.K. Law, S. Menon, Simulation of soot formation in turbulent premixed flames, Combust. Flame 150 (1–2) (2007) 108–126.
[18] H. El-Asrag, S. Menon, Large eddy simulation of soot formation in a turbulent non-premixed jet flame, Combust. Flame 156 (2) (2009) 385–395.
[19] M.E. Mueller, H. Pitsch, Large eddy simulation subfilter modeling of soot-turbulence interactions, Phys. Fluids 23 (11) (2011) 115104.
[20] S. Navarro-Martinez, S. Rigopoulos, Differential diffusion modelling in LES with RCCE-reduced chemistry, Flow Turbul. Combust. 89 (2) (2012) 311–328.
[21] M.E. Mueller, H. Pitsch, LES model for sooting turbulent nonpremixed flames, Combust. Flame 159 (6) (2012) 2166–2180.
[22] P. Donde, V. Raman, M.E. Mueller, H. Pitsch, LES/PDF based modeling of soot–turbulence interactions in turbulent flames, Proc. Combust. Inst. 34 (1) (2013) 1183–1192.
[23] M.E. Mueller, Q.N. Chan, N.H. Qamar, B.B. Dally, H. Pitsch, Z.T. Alwahabi, G.J. Nathan, Experimental and computational study of soot evolution in a turbulent nonpremixed bluff body ethylene flame, Combust. Flame 160 (7) (2013) 1298–1309.
[24] M.E. Mueller, H. Pitsch, Large eddy simulation of soot evolution in an aircraft combustor, Phys. Fluids 25 (11) (2013) 110812.
[25] H. Koo, M. Hassanaly, V. Raman, M.E. Mueller, K.P. Geigle, Large-Eddy simulation of soot formation in a model gas turbine combustor, J. Eng. Gas Turbine Power 139 (3) (2017) 031503.
[26] C. Eberle, P. Gerlinger, K.P. Geigle, M. Aigner, Toward finite-rate chemistry large-eddy simulations of sooting swirl flames, Combust. Sci. Technol. 190 (7) (2018) 1194–1217.
[27] F. Sewerin, S. Rigopoulos, An LES-PBE-PDF approach for predicting the soot particle size distribution in turbulent flames, Combust. Flame 189 (2018) 62–76.
[28] P. Rodrigues, B. Franzelli, R. Vicquelin, O. Gicquel, N. Darabiha, Coupling an LES approach and a soot sectional model for the study of sooting turbulent non-premixed flames, Combust. Flame 190 (2018) 477–499.
[29] A. Giusti, E. Mastorakos, C. Hassa, J. Heinze, E. Magens, M. Zedda, Investigation of flame structure and soot formation in a single sector model combustor using experiments and numerical simulations based on the large eddy simulation/conditional moment closure approach, J. Eng. Gas Turbine Power 140 (6) (2018) 061506.
[30] W. Han, V. Raman, M.E. Mueller, Z. Chen, Effects of combustion models on soot formation and evolution in turbulent nonpremixed flames, Proc. Combust. Inst. 37 (1) (2019) 985–992.
[31] A. Jain, Y. Xuan, Effects of large aromatic precursors on soot formation in turbulent non-premixed sooting jet flames, Combust. Theor. Model. 23 (3) (2019) 439–466.
[32] S. Yang, J.K. Lew, M.E. Mueller, Large eddy simulation of soot evolution in turbulent reacting flows: presumed subfilter PDF model for soot-turbulence–chemistry interactions, Combust. Flame 209 (2019) 200–213.
[33] S. Gkantonas, M. Sirignano, A. Giusti, A. D'Anna, E. Mastorakos, Comprehensive soot particle size distribution modelling of a model Rich-Quench-Lean burner, Fuel 270 (2020) 117483.
[34] M. Grader, C. Eberle, P. Gerlinger, Large-eddy simulation and analysis of a sooting lifted turbulent jet flame, Combust. Flame 215 (2020) 458–470.
[35] K. Netzell, H. Lehtiniemi, F. Mauss, Calculating the soot particle size distribution function in turbulent diffusion flames using a sectional method, Proc. Combust. Inst. 31 (1) (2007) 667–674.
[36] V. Fraioli, C. Beatrice, M. Lazzaro, Soot particle size modelling in 3D simulations of diesel engine combustion, Combust. Theor. Model. 15 (6) (2011) 863–892.
[37] D. Aubagnac-Karkar, J.B. Michel, O. Colin, P.E. Vervisch-Kljakic, N. Darabiha, Sectional soot model coupled to tabulated chemistry for diesel RANS simulations, Combust. Flame 162 (8) (2015) 3081–3099.
[38] D. Aubagnac-Karkar, J.B. Michel, O. Colin, N. Darabiha, Combustion and soot modelling of a high-pressure and high-temperature dodecane spray, Int. J. Engine Res. 19 (4) (2018) 434–448.
[39] M.A. Schiener, R.P. Lindstedt, Joint-scalar transported PDF modelling of soot in a turbulent non-premixed natural gas flame, Combust. Theor. Model. 22 (6) (2018) 1134–1175.
[40] M.A. Schiener, R.P. Lindstedt, Transported probability density function based modelling of soot particle size distributions in non-premixed turbulent jet flames, Proc. Combust. Inst. 37 (1) (2019) 1049–1056.
[41] L. Tian, M.A. Schiener, R.P. Lindstedt, Fully coupled sectional modelling of soot particle dynamics in a turbulent diffusion flame, Proc. Combust. Inst. 38 (1) (2021) 1365–1373.
[42] M. Ihme, H. Pitsch, Modeling of radiation and nitric oxide formation in turbulent nonpremixed flames using a flamelet/progress variable formulation, Phys. Fluids 20 (5) (2008) 055110.
[43] T.W.J. Peeters, P.P.J. Stroomer, J.E. de Vries, D.J.E.M. Roekaerts, C.J. Hoogendoorn, Comparative experimental and numerical investigation of a piloted turbulent natural-gas diffusion flame, Symp. (Int.) Combust. 25 (1) (1994) 1241–1248.
[44] K.M. Leung, R.P. Lindstedt, W.P. Jones, A simplified reaction mechanism for soot formation in nonpremixed flames, Combust. Flame 87 (3–4) (1991) 289–305.
[45] E.E. O'Brien, The probability density function (pdf) approach to reacting turbulent flows, in: P.A. Libby, F.A. Williams (Eds.), Turbulent Reacting Flows, Springer Berlin Heidelberg, Berlin, Heidelberg (1980), pp. 185–218.
[46] S.B. Pope, PDF methods for turbulent reactive flows, Prog. Energy Combust. Sci. 11 (2) (1985) 119–192.
[47] W.P. Jones, The joint scalar probability density function method, in: B.E. Launder, N.D.E. Sandham (Eds.), Closure Strategies for Turbulent and Transitional Flows, Cambridge University Press (2002), pp. 582–625.

[48] D.C. Haworth, Progress in probability density function methods for turbulent reacting flows, Prog. Energy Combust. Sci. 36 (2) (2010) 168–259.
[49] L. Valiño, Field Monte Carlo formulation for calculating the probability density function of a single scalar in a turbulent flow, Flow Turbul. Combust. 60 (2) (1998) 157–172.
[50] G. Hauke, L. Valiño, Computing reactive flows with a field Monte Carlo formulation and multi-scale methods, Comput. Methods Appl. Mech. Eng. 193 (15) (2004) 1455–1470.
[51] V. Sabel'nikov, O. Soulard, Rapidly decorrelating velocity-field model as a tool for solving one-point Fokker-Planck equations for probability density functions of turbulent reactive scalars, Phys. Rev. E 72 (1) (2005) 016301.
[52] J. Villermaux, J.C. Devillon, Représentation de la coalescence et de la redispersion des domaines de ségrégation dans un fluide par un modèle d'interaction phénoménologique, Proceedings of the 2nd International Symposium on Chemical Reaction Engineering, volume 26, Elsevier, New York (1972), pp. 1–13.
[53] C. Dopazo, E.E. O'Brien, An approach to the autoignition of a turbulent mixture, Acta Astronaut. 1 (9–10) (1974) 1239–1266.
[54] S. Rigopoulos, PDF method for population balance in turbulent reactive flow, Chem. Eng. Sci. 62 (23) (2007) 6865–6878.
[55] G.Y. Di Veroli, S. Rigopoulos, Modeling of turbulent precipitation: a transported population balance-PDF method, AIChE J. 56 (4) (2010) 878–892, doi:10.1002/aic.12064.
[56] G.Y. Di Veroli, S. Rigopoulos, Modeling of aerosol formation in a turbulent jet with the transported population balance equation-probability density function approach, Phys. Fluids 23 (4) (2011) 043305.
[57] F. Sewerin, S. Rigopoulos, An LES-PBE-PDF approach for modeling particle formation in turbulent reacting flows, Phys. Fluids 29 (10) (2017) 105105.
[58] W. Kollmann, I.M. Kennedy, M. Metternich, J.-Y. Chen, Application of a soot model to a turbulent ethylene diffusion flame, in: H. Bockhorn (Ed.), Soot Formation in Combustion, Springer Series in Chemical Physics 59, Springer-Verlag (1994), pp. 503–526.
[59] I.M. Aksit, J.B. Moss, A hybrid scalar model for sooting turbulent flames, Combust. Flame 145 (1–2) (2006) 231–244.
[60] R.P. Lindstedt, S.A. Louloudi, Joint-scalar transported PDF modeling of soot formation and oxidation, Proc. Combust. Inst. 30 (1) (2005) 775–782.
[61] J.L. Consalvi, F. Nmira, Effects of soot absorption coefficient-Planck function correlation on radiative heat transfer in oxygen-enriched propane turbulent diffusion flame, J. Quant. Spectrosc. Radiat. Transfer 172 (2016) 50–57.
[62] B. Zamuner, F. Dupoirieux, Numerical simulation of soot formation in a turbulent flame with a Monte-Carlo PDF approach and detailed chemistry, Combust. Sci. Technol. 158 (2000) 407–438.
[63] G. Blanquart, P. Pepiot-Desjardins, H. Pitsch, Chemical mechanism for high temperature combustion of engine relevant fuels with emphasis on soot precursors, Combust. Flame 156 (3) (2009) 588–607.
[64] G. Blanquart, H. Pitsch, A joint volume-surface-hydrogen multi-variate model for soot formation, in: H. Bockhorn, A. D'Anna, A. Sarofim, H. Wang (Eds.), Combustion Generated Fine Carbonaceous Particles, KIT Scientific Publishing (2009), pp. 437–463.
[65] A. Liu, S. Rigopoulos, A conservative method for numerical solution of the population balance equation, and application to soot formation, Combust. Flame 205 (2019) 506–521.
[66] J.Y. Zhang, C.R. Shaddix, R.W. Schefer, Design of "model-friendly" turbulent non-premixed jet burners for c2+ hydrocarbon fuels, Rev. Sci. Instrum. 82 (7) (2011) 074101.
[67] B. Sun, S. Rigopoulos, A. Liu, Modelling of soot coalescence and aggregation with a two-population balance equation model and a conservative finite volume method, Combust. Flame 229 (2021) 111382.
[68] S.K. Friedlander, Smoke, Dust, and Haze: Fundamentals of Aerosol Dynamics, 2nd ed., Oxford University Press, 2000.
[69] W.P. Jones, V.N. Prasad, Large Eddy Simulation of the Sandia Flame Series (D–F) using the Eulerian stochastic field method, Combust. Flame 157 (9) (2010) 1621–1636.
[70] J. Smagorinsky, General circulation experiments with the primitive equations: I. The basic experiment, Mon. Weather Rev. 91 (3) (1963) 99–164.
[71] F. Gao, E.E. O'Brien, A large-eddy simulation scheme for turbulent reacting flows, Phys. Fluids A 5 (6) (1993) 1282–1284.
[72] S.B. Pope, Turbulent Flows, Cambridge University Press, 2000.
[73] R.O. Fox, Computational Models for Turbulent Reacting Flows, Cambridge Series in Chemical Engineering, Cambridge University Press, 2003.
[74] R. McDermott, S.B. Pope, A particle formulation for treating differential diffusion in filtered density function methods, J. Comput. Phys. 226 (1) (2007) 947–993.
[75] V.N. Prasad, Large Eddy Simulation of Partially Premixed Turbulent Combustion, Imperial College London, 2011 Ph.D. thesis.
[76] S. Mitarai, J.J. Riley, G. Kosály, Testing of mixing models for Monte Carlo probability density function simulations, Phys. Fluids 17 (4) (2005) 047101.
[77] S.B. Pope, A Monte Carlo method for the PDF equations of turbulent reactive flow, Combust. Sci. Technol. 25 (5–6) (1981) 159–174.
[78] G.A. Pavliotis, Stochastic Processes and Applications, Springer-Verlag New York, 2014.
[79] M.F. Modest, Radiative Heat Transfer, 3rd ed., Academic Press, 2013.
[80] M. Frenklach, H. Wang, Detailed modeling of soot particle nucleation and growth, Symp. (Int.) Combust. 23 (1) (1991) 1559–1566.
[81] O. Link, D.R. Snelling, K.A. Thomson, G.J. Smallwood, Development of absolute intensity multi-angle light scattering for the determination of polydisperse soot aggregate properties, Proc. Combust. Inst. 33 (2011) 847–854.
[82] A.M. Brasil, T.L. Farias, M.G. Carvalho, A recipe for image characterization of fractal-like aggregates, J. Aerosol. Sci. 30 (10) (1999) 1379–1389.
[83] M. Schenk, S. Lieb, H. Vieker, A. Beyer, A. Gölzhäuser, H. Wang, K. Kohse-Höinghaus, Morphology of nascent soot in ethylene flames, Proc. Combust. Inst. 35 (2) (2015) 1879–1886.
[84] W.P. Jones, F. di Mare, A.J. Marquis, LES-BOFFIN: User's Guide, 2002.
[85] F. Sewerin, S. Rigopoulos, Algorithmic aspects of the LES-PBE-PDF method for modeling soot particle size distributions in turbulent flames, Combust. Sci. Technol. 191 (5–6) (2019) 766–796.
[86] R. Mustata, L. Valiño, C. Jiménez, W.P. Jones, S. Bondi, A probability density function Eulerian Monte Carlo field method for large eddy simulations: application to a turbulent piloted methane/air diffusion flame (sandia d), Combust. Flame 145 (1–2) (2006) 88–104.
[87] W.P. Jones, S. Navarro-Martinez, Large eddy simulation of autoignition with a subgrid probability density function method, Combust. Flame 150 (3) (2007) 170–187.
[88] S.P. Kearney, D.R. Guildenbecher, C. Winters, P.A. Farias, T.W. Grasser, J.C. Hewson, Temperature, Oxygen, and Soot-Volume-Fraction Measurements in a Turbulent C_2H_4-Fueled Jet Flame, Technical Report, Sandia National Laboratories, 2015. SAND2015-7968
[89] C.R. Shaddix, J. Zhang, R.W. Schefer, J. Doom, J.C. Oefelein, S. Kook, L.M. Pickett, H. Wang, Understanding and Predicting Soot Generation in Turbulent Non-Premixed Jet Flames, Technical Report, Sandia National Laboratories, 2010. SAND2010-7178
[90] International Sooting Flame (ISF) Workshop, 2018, https://www.adelaide.edu.au/cet/isfworkshop/.
[91] M. Kholghy, A. Veshkini, M.J. Thomson, The core-shell internal nanostructure of soot - a criterion to model soot maturity, Carbon 100 (2016) 508–536.
[92] A. Veshkini, S.B. Dworkin, M.J. Thomson, A soot particle surface reactivity model applied to a wide range of laminar ethylene/air flames, Combust. Flame 161 (12) (2014) 3191–3200.
[93] W. Boyette, S. Chowdhury, W. Roberts, Soot particle size distribution functions in a turbulent non-premixed ethylene-nitrogen flame, Flow Turbul. Combust. 98 (2017) 1173–1186.
[94] S. Chowdhury, W.R. Boyette, W.L. Roberts, Time-averaged probability density functions of soot nanoparticles along the centerline of a piloted turbulent diffusion flame using a scanning mobility particle sizer, J. Aerosol. Sci. 106 (2017) 56–67.
[95] M. Lucchesi, A. Abdelgadir, A. Attili, F. Bisetti, Simulation and analysis of the soot particle size distribution in a turbulent nonpremixed flame, Combust. Flame 178 (2017) 35–45.
[96] S.B. Pope, Computationally efficient implementation of combustion chemistry using in situ adaptive tabulation, Combust. Theor. Model. 1 (1) (1997) 41–63.
[97] G. Ribert, L. Vervisch, P. Domingo, Y.-S. Niu, Hybrid transported-tabulated strategy to downsize detailed chemistry for numerical simulation of premixed flames, Flow Turbul. Combust. 92 (1–2) (2014) 175–200.
[98] B. Duboc, G. Ribert, P. Domingo, Hybrid transported-tabulated chemistry for partially premixed combustion, Comput. Fluids 179 (2019) 206–227.
[99] L.L.C. Franke, A.K. Chatzopoulos, S. Rigopoulos, Tabulation of combustion chemistry via artificial neural networks (ANNs): methodology and application to LES-PDF simulation of sydney flame l, Combust. Flame 185 (2017) 245–260.
[100] T. Readshaw, T. Ding, S. Rigopoulos, W.P. Jones, Modelling of turbulent flames with the Large Eddy Simulation - probability density function (LES-PDF) approach, stochastic fields and artificial neural networks, Phys. Fluids 33 (2021) 035154.
[101] T. Ding, T. Readshaw, S. Rigopoulos, W.P. Jones, Machine learning tabulation of thermochemistry in turbulent combustion: an approach based on hybrid flamelet/random data and multiple multilayer perceptrons, Combust. Flame 231 (2021) 111493.
[102] A. Seltz, P. Domingo, L. Vervisch, Solving the population balance equation for non-inertial particles dynamics using probability density function and neural networks: application to a sooting flame, Phys. Fluids 33 (1) (2021) 013311.